A NUMERICAL STUDY OF THE MID-FIELD RIVER PLUME

A Dissertation

by

KELLY LYNNE COLE

Submitted to the Office of Graduate Studies of
Texas A&M University
in partial fulfillment of the requirements for the degree of

DOCTOR OF PHILOSOPHY

Chair of Committee,	Robert Hetland
Committee Members,	Ping Chang
	David Brooks
	Scott Socolofsky
	Daniel MacDonald
Department Head,	Debbie Thomas

May 2014

Major Subject: Oceanography

ABSTRACT

Idealized and realistic simulations of the Merrimack River plume on the east coast of the U.S. are performed using the Regional Ocean Modeling System (ROMS). The effect of discharge, tides and rotation on the evolution of the tidal plume are examined. Experiments investigating the deceleration of the plume body through mixing and the relaxation of the tidal plume front are performed. Three primary findings result from this research. First, more ambient water interacts with the tidal plume front than source water. Because it takes several hours for source water to translate the plume and it is strongly diluted in the plume interior, only a small fraction of source water reaches the front. Therefore, the front is responsible for a small portion of mixing of the total ebb discharge. Second, the mouth and the tidal plume front communicate on an advective time scale. When the ebb discharge is stopped at the estuary mouth, the inertia of the discharge is enough to keep previously released source water necessary to sustain frontal propagation moving frontward. The front begins to slow when the withheld estuarine discharge is not supplied to the front. Third, the net plume mixing, defined as the total mixing of a parcel of source water before it enters the far-field, is altered by rotation. As discharge increases, an irrotational plume will exhibit an increasing trend in net mixing, while a rotational plume will exhibit a decreasing trend. These experiments bridge engineering and geophysical scale plume studies and provide a framework for understanding results reported in literature.

DEDICATION

For my sister, Paige, who assures me that if I submit a paper from her balcony with a Pacific view then I'm sure to get an 'A'.

ACKNOWLEDGEMENTS

I owe the completion of this dissertation to many. This research is part of the Merrimack River Mixing and Divergence Experiment (MeRMADE), funded by project National Science Foundation grant 0850622. National Science Foundation STEM Contract DUE-0806926 has also contributed greatly to my graduate education.

I want to thank my committee chair, Rob Hetland, for introducing me to ocean dynamics, and more importantly, good music. I'm forever grateful I crashed his seminar on installing ROMS in my first year of grad school; as I only have before in the presence of inspiring masterpieces at art museums, the upwelling case flowing in Ncview made me cry a little. I'm extremely fortunate to have had the best training as a modeler and scientist working with Rob. I also want to thank my committee members Ping Chang, Dave Brooks, Scott Socolofsky and Dan MacDonald for their insight and direction in my research.

I want to thank the MeRMADE group: Rob Hetland, Dan MacDonald, Alex Horner-Devine, Yeping Yuan and Georgia Kakoulaki for many useful plume discussions and guidance in writing this manuscript. I especially want to thank Georgia Kakoulaki for the happy times on the Mary D, storming castles in the dark to find drifters and other, mud-sinking, boot-losing, salt marsh adventures.

Many of the research ideas presented in this dissertation are a result of insightful discussions amongst the Physical Oceanography Numerical Group, whom I must thank for both academic support and friendship. I especially want to thank the Zhangs: Zhaoru, Wenxia and XQ for making me an honorary Zhang.

My friends and family have witnessed the sweat and tears it took to create this document; they've shared them with me, and together we've learned that these are

truly the most powerful forces of fluid. Thank you for the love and support you've always provided.

TABLE OF CONTENTS

Page

LIST OF FIGURES

FIGURE Page

LIST OF TABLES

1. INTRODUCTION

Approximately 2.5% of water on Earth is fresh water, and of this, about 0.006% exists in rivers (Covich et al., 1993). Approximately one-third of the precipitation over land, 4 x 10^3 km^3 yr^{-1} of fresh water over the globe, is transported into the ocean via rivers (Trenberth et al., 2007; Allison et al., 2014). Although the amount of fresh water that enters the ocean in river plumes is small, it has an immense impact on the ecological health of coastal regions, and thus the utility of nearshore resources, including food, energy, transportation and recreation, therefore understanding how riverine fresh water stratifies, mixes with and ultimately becomes ocean water is necessary to make wise management decisions.

River plumes deliver anthropogenic nutrients and sediment that influence biogeochemical processes at the coast (Allison et al., 2014). For example, seasonal hypoxic conditions exist on the TX-LA shelf where the Mississippi River delivers ample fresh water, stratifying the shelf and preventing vertical mixing and ventilation of bottom water (Hetland and DiMarco, 2008). Furthermore, the Mississippi transports nutrients cast off from farmlands of the Midwest, US to the coastal ocean that are consumed by plankton, initializing a bloom that, upon death, sustains bacteria in the water column that utilize oxygen (Turner and Rabalais, 1994). Since these biogeochemical processes are tightly linked to estuarine and coastal dynamics in the region of freshwater influence, it is important to investigate the physical evolution of river plumes.

Perhaps the most important governing variables of plume dynamics offshore are river discharge magnitude and the geometry of the coast at the estuary mouth (Hetland, 2010). Between different river systems, discharge can vary by five orders of magnitude, and discharge typically varies by at least one order of magnitude seasonally for a single river (Allison et al., 2014). Physical characteristics of the discharge govern the evolution of a plume offshore. Many narrow mouth, geophysical scale fresh water plumes are surface trapped (Yankovsky and Chapman, 1997). These plumes develop when the fresh layer detaches from the bottom near the mouth, shoals and spreads laterally, with no bottom interaction seaward of the lift-off point. Bottom trapped plumes, however, occur when the emergent plume layer stays attached to the ocean bottom. Surface advection is common in plumes with a large buoyancy anomaly and low to medium discharge, as higher discharge tends to keep a plume attached to the bottom offshore. The plume-induced vertical and horizontal shelf stratification impacts biological activity through impeding vertical migration or enhancing alongshore transport.

The goal of this research is to increase understanding of buoyancy driven flow in the coastal ocean, namely the spatial structure and temporal evolution of the Merrimack River plume, a tidally modulated, medium discharge, surface advected, narrow mouth plume in the Gulf of Maine. New information about plume mixing, spreading and the transmission of source water form the estuary mouth to the plume front will improve predictive capabilities in nearshore regions and ultimately facilitate coastal water quality management.

1.1 Background

How are plumes compared over a large parameter space? In this section, classification of plumes based on horizontal spatial structure using inflow length scales is introduced. Also, analysis of plume structure and mixing in isohaline space is presented as a method to decompose plumes into dynamic regions.

1.1.1 Non-dimensional numbers

The Burger, Rossby and Froude numbers are non-dimentional numbers that describe plume behavior. When calculated at the inflow, they provide estimates of the plume structure offshore. These numbers give the relative importance of buoyancy, inertia and rotation to the flow. The inflow Burger number is similar to the mouth Kelvin number and defined as the width of the estuary mouth relative to the internal deformation scale for density induced flow (O'Donnell, 1990; Münchow and Garvine, 1993; Garvine, 1995; Yankovsky and Chapman, 1997; Valle-Levinson, 2008; Huq, 2009). $R_d = \sqrt{g'h}/f$ is the baroclinic Rossby radius of the inflow, where f is the rotational frequency, $g' = g\Delta\rho/\rho_0$ and h are reduced gravity and depth at the estuary mouth, g is gravity, $\Delta\rho$ is the inflow density anomaly and ρ_0 is the ambient density. $S = R_d/W$ is the Burger number of the inflow, where W is the mouth width, $R_o = U/fW$ is the inflow Rossby number, where U is the mean velocity of the inflow, and $Fr = R_o/S = U/\sqrt{g'h}$ is the inflow Froude number. Large values for R_o and S indicate that rotation has little effect near the source; a small mouth width significantly constricts the flow, creating a strong jet-like discharge. Narrow mouth estuaries with a large Burger number possess a contraction that chokes the estuarine outflow and acts as an internal hydraulic control that governs the exchange flow (Armi and Farmer, 1986). These estuaries produce plumes that expand radially and form a bulge. In estuaries with wide mouths relative to the deformation radius, rotation affects the flow before fresh water leaves the estuary and lateral variations in inflow parameters across the mouth develop that alter spreading and mixing, creating plumes with different density structure than large inflow Burger number plumes. If the inflow Froude number is subcritical, the buoyancy of the inflow influences plume evolution more than advection; this is evidenced by the formation of a surface advected plume. Theoretically, If the Froude number is supercritical, advection dominates over buoyancy and a bottom trapped plume forms (Yankovsky and Chapman, 1997). This seems counterintuitive since most supercritical outflows form a surface trapped plume. Even these plumes are attached to the bottom for some time after leaving the estuary, lift off, and become a surface plume. The formation of a bottom attached plume at supercritical discharge is illustrated, for example, by the Mississippi; a discharge of such magnitude that it stays in contact with the bottom for several kilometers offshore, lifting off when it encounters steep bathymetry (W. Zhang, personal communication).

1.1.2 Length scales of the inflow

During early plume formation, the geometry of the mouth, and momentum and buoyancy fluxes of the discharge determine the spatial extent of the jet-like estuarine outflow on the shelf. For several hours over ebb, during which steady conditions can be assumed, buoyant discharge leaves the source as a jet, and at some location offshore, lifts off from the ocean bottom as a plume. Jones et al. (2007) describes classification of engineering scale flows (irrotational, with a mouth width-to-depth aspect ratio $\mathcal{O}(1)$) by their jet/plume-like behavior and bottom/shoreline interaction based on coastline geometric conditions and four key length scales determined from inflow and ambient characteristics: the discharge length sale, jet-to-plume-length scale, jet-to-crossflow length scale and plume-to-crossflow length scale. The jet-to-plume length scale is defined as $L_M = M_i^{\frac{3}{4}} J_i^{-\frac{1}{2}}$, where $M_i = U^2 W h$ is the momentum flux and $J_i = g' U W h$ is the buoyancy flux of the inflow. The jet-to-plume length scale would appear to be the most significant for a geophysical plume like the Merrimack because it can be used as a scale for the near-field (see Section 1.1.4.2). The jet-to-plume length scale determines where the discharge transitions from jet-like flow to a plume-like density current where entrainment mechanisms are distinctly different. Diffusion of momentum in the jet causes the transition between the jet and potential type flow where buoyancy becomes important and spreading prevails (Kashiwamura and Yoshida, 1967; Wright and Coleman, 1971; Jones et al., 2007). In the Merrimack, the near field typically spans the first few kilometers near the river mouth; the jet-to-plume length scale generally predicts a much smaller near-field on the order of meters, likely because of the difficulty applying these predictive length scales to a tidally pulsed, geophysical scale plume.

While initial fluxes are inarguably important factors in a plume's early formation, engineering theory is difficult to apply to geophysical scale plumes because of the difference in source aspect ratios, which is much smaller for geophysical scale plumes. Additionally, in the geophysical case there are rotational effects even near the estuary mouth. The length scales presented in Jones et al. (2007) and Jirka (2007) describe the plume in Cartesian space, but isohaline space, described in the next section, is a more reliable coordinate system to use because it moves with the plume (Hetland, 2005).

1.1.3 Salinity coordinates

An isohaline-based coordinate system is useful because it expands and translates with the plume. Fresh water can be tracked through salinity space to identify the isohalines where it pools and where it is flushed to saltier isohalines by vigorous mixing with background waters, and dynamic plume regions can be inferred from this distribution of fresh water in salinity coordinates (Hetland, 2005).

Consider the volume V, bounded at the river end by a vertical cross section where $s = 0$ and bounded at the ocean end by an isohaline surface area A, where $s = s_A$. The region V is bounded above by the sea surface and below by the ocean bottom. Fig. 1.1 shows a schematic of V (red region). Following the formulation in MacCready et al. (2002) and Hetland (2005) and using the approach described on pp. 74 - 76 in Kundu (1990), the time rate of change of the volume V is given by

$$\frac{\partial V}{\partial t} + \int_A \mathbf{u} \cdot \hat{\mathbf{n}} \, dA - \int_A \mathrm{u}_A \, dA = Q_f, \tag{1.1}$$

where $\mathbf{u}$ is the three-dimensional fluid velocity vector, $\hat{\mathbf{n}}$ is the unit surface normal vector to A, u_A is the normal velocity of the surface A and Q_f is the fresh water flux through the cross section $s = 0$ at the river mouth. Similarly, the three-dimensional salt balance equation integrated over volume V is given by

$$\frac{\partial}{\partial t} \int_V s \, dV + s_A \int_A \mathbf{u} \cdot \hat{\mathbf{n}} \, dA - s_A \int_A \mathrm{u}_A \, dA = - \int_A \mathbf{F} \cdot \hat{\mathbf{n}} \, dA, \tag{1.2}$$

where $\mathbf{F}$ is the turbulent salt flux vector. Combining the volume and salt balance equations gives

$$\frac{\partial}{\partial t} \int_V s \, dV - s_A \frac{\partial V}{\partial t} + s_A Q_f = - \int_A \mathbf{F} \cdot \hat{\mathbf{n}} \, dA. \tag{1.3}$$

Assuming a steady river discharge and salinity field in the plume, which is reasonable over several hours of ebb, gives

$$s_A Q_f = - \int_A \mathbf{F} \cdot \hat{\mathbf{n}} \, dA. \tag{1.4}$$

The physical meaning of Eq. (1.4) is that fresh water added at the river end of the volume V is balanced by the turbulent flux of fresh water $\mathbf{F}/s_A$ across A, describing an advective-diffusive balance in the estuary-plume system (MacCready et al., 2002). The cartoon in Fig. 1.1 illustrates this idea. The cartoon depicts a vertical section through the core of the plume during ebb. Q_f is the river discharge rate; the fresh water flowing into the plume at high velocities and spreading at the ocean surface causes shear instabilities at the plume base, identified by the curled arrows showing mixing between the plume and ocean water ($\int_A \mathbf{F} \cdot \hat{\mathbf{n}}\, dA \neq 0$). Dense, dark gray arrows indicate vigorous mixing. The strength of mixing decreases offshore and the isohalines expand. To infer dynamic plume regions from the isohaline structure, the mixing between plume isohalines and ocean water at the pycnocline across A must be evaluated and related to near- and far-field mixing rates.

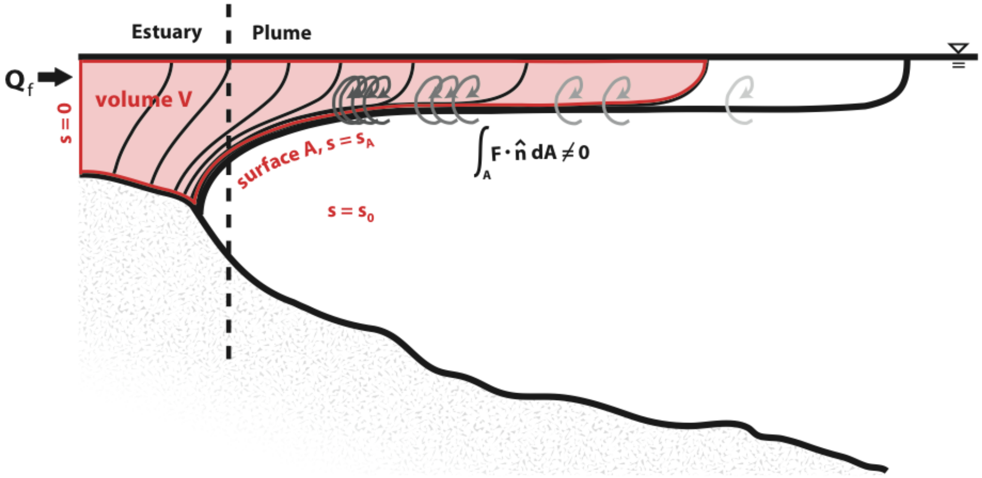

Figure 1.1: Cartoon illustrating plume isohaline vertical structure. Black lines are isohalines. The red region is the isohaline volume V bounded by surface A, described in Eq. (1.1) - Eq. (1.4). Q_f is the fresh water discharge and $\int_A \mathbf{F} \cdot \hat{\mathbf{n}}\, dA \neq 0$ indicates turbulent mixing across surface A. Dark gray curled arrows represent strong entrainment and light gray curled arrows represent weak entrainment. Dotted line marks the separation between the estuary and plume.

1.1.4 Dynamic plume regions

The jet-like region in the first few kilometers of the estuary mouth is the near-field plume. Fresh water flows through this region within a few hours and changes in salinity are large because of intense shear mixing (MacDonald et al., 2007) (note the isohalines close together near the river mouth in Fig. 1.1, indicating a rapid change in salinity). Fig. 1.2 shows a schematic of the dynamic regions of a coastal plume, representing the Merrimack River plume (D. MacDonald, R. Hetland and A. Horner-Devine, unpubl.). The near-field is the region in the orange box.

As the near-field scales with the deformation radius, geostrophic adjustment occurs through the cross shore density gradient (Chapman and Lentz, 1994, 1997; Yankovsky and Chapman, 1997; Whitney and Garvine, 2005). Plume spreading and shear mixing is arrested, and streamlines are redirected parallel to the front (and coast) as the plume turns anticyclonically, creating the far-field. The far-field is the plume region where rotation dominates the circulation; it is composed of the geostrophic coastal current that flows downcoast of the river mouth. Because of the rotational influence, the far-field exhibits longer time scales than the near-field; fresh water is moved through the far-field over several days. In addition, wind mixes plume and ocean water and advects the far-field through an Ekman balance (Fong and Geyer, 2001, 2002; Garcia Berdeal et al., 2002; Whitney and Garvine, 2005; Hetland, 2005; Choi and Wilkin, 2007).

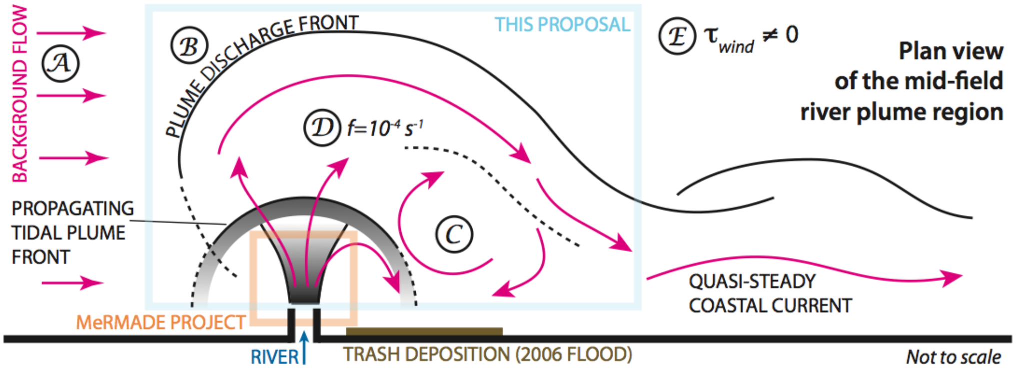

Figure 1.2: Schematic from (D. MacDonald, R. Hetland and A. Horner-Devine, unpubl.) showing plume regions and physical forcings in the Merrimack River plume. The orange box marks the near-field and the blue box extends the study area into the mid-field; the focus of this project.

1.1.4.1 Plume inflow conditions

The importance of initial flow conditions at the estuary mouth to plume evolution is well established in literature (see Section 1.1.1 and Section 1.1.2). Estuarine mixing processes and two-layer flow hydraulics set the exchange of river and ocean water at the mouth; tides modulate the exchange and can affect it through mixing within the estuary, as they are an important part of dissipation and transfer of energy to the density field (MacCready, 1999; Zhong and Li, 2006; MacCready, 2007; MacCready et al., 2009). Buoyancy driven processes combine with mechanical processes in estuarine shallow, stratified shear environments, and the resultant estuarine water mass acts as a boundary condition for the plume. Mixing in estuaries is caused by near-bed flows over the rough bottom and protuberant topographic features and through internal shear layers.

1.1.4.2 Mixing and spreading in the near-field

Spreading occurs when a buoyant parcel of water leaves the narrow estuary, enters the ocean, and encounters strong lateral density gradients, expanding the plume radially behind a front that moves offshore due to the hydraulic gradient between the plume and ambient water. The plume layer shoals and accelerates, spreading radially at a rate related to the local internal gravity wave phase speed (Wright and Coleman, 1971; Hetland and MacDonald, 2008).

Mixing in near-field jets and plumes is achieved through entrainment of the surrounding ambient fluid. Jirka (2007) describe distinct momentum and mass entrainment processes that occur in the near field; all have separate parameterizations in the model used in their study. Pure plume, pure jet, pure wake and advected line puffs are several entrainment regimes (Jirka, 2004). The existence and growth of these regimes is determined by the relative importance of initial momentum and buoyancy at the jet source as well as ambient flow characteristics (Chu, 1997). Horizontal entrainment, vertical entrainment and advected puff entrainment occur in the pure jet-like region of the discharge while interfacial and frontal entrainment occur in the buoyant plume-like region. Several entrainment formulations include a Richardson number dependent factor, where buoyancy damps the entrainment rate. The near-field is terminated when flow in the plume becomes subcritical, and entrainment is supressed (MacDonald et al., 2007; McCabe et al., 2008; Kilcher et al., 2012).

Mixing and spreading are opposing processes in the near field; spreading increases the velocity of the upper layer and leads to shear mixing at the plume-ambient interface, but mixing damps the spreading because it reduces the plume density anomaly (Chen and MacDonald, 2006). Mixing decreases the upper layer Froude number while spreading increases the upper layer Froude number (Hetland and MacDonald, 2008).

1.1.4.3 The mid-field transition

Offshore of the buoyancy-and-advection-dominated near-field region, before the plume transitions into a far-field geostrophic coastal current, plume dynamics consist of an amalgam of these two regimes. This is the mid-field plume region, where tidal currents, ambient currents, wind and rotation begin to divert the plume from its offshore course. Fig. 1.2 illustrates the physical forcings that govern the mid-field.

Previous studies of buoyant plumes focus on near- and far-field behavior separately, therefore the relative significance of river discharge rate, wind, tides, ambient flow and rotation to plume evolution through the mid-field transition is not well understood. Net plume properties established in the near-field govern plume evolution offshore because the near-field acts as the boundary condition for the mid- and far-field plumes; therefore, a goal of this project is to quantify net plume properties through the near-field.

Feedback between the three regions is intensified in the presence of tides. In a tidally pulsed regime, the far-field plume receives the new ebb discharge, and the stratification of older, far-field plume water on the shelf impacts mixing in the near-field plume. Similarly, the water released early in ebb sets the initial stratification conditions in the plume interior for source water released later in ebb, feeding back into the complex near-field mixing and spreading relationship that affects source water supplied to the mid- and far-field plumes.

1.1.4.4 Tidally pulsed inflow

Natural variability in the timing and magnitude of fresh water discharge occurs in coastal environments (Pritchard and Huntley, 2006). During each ebb, buoyant water leaves the source and forms a new plume. The ebb pulse of estuarine water embodies the tidal plume (the near-field is pulsed with the tidal plume); recent, previous tidal pulses form a recirculation of fresh water on the shelf that the tidal plume meets (a component of the mid-field), while remnants of the oldest tidal pulses on the shelf comprise the far-field plume (Horner-Devine et al., 2009). During each ebb, the new tidal plume transfers buoyancy downward as it flows over the recirculating and far-field plumes, and as ebb ends it is assimilated into older plume waters (Horner-Devine et al., 2009). The tidal plume sets the stage for plume dynamics seaward of the mouth because it is where significant mixing takes place at the source, the near-field and front, establishing the upper layer density anomaly for the far-field plume (Hetland, 2010). The physical forcings shown in Fig. 1.2, along with the geometry of the mouth, determine the existence and temporal evolution of the tidal plume, as it's arrest indicates the mid-field transition.

1.2 Physical environment of the Merrimack estuary and plume

This study combines idealized and realistic numerical simulations of the Merrimack River plume just south of the Massachusetts-New Hampshire border. It is an ideal location to establish plume paradigms because of its relatively simple dynamics due to the narrow estuary, uncomplicated geometry of the mouth and coast, and shelf bathymetry. Furthermore, much insight into the physical processes of this region can be gained from an idealized modeling study because of these uncomplicated features. A detailed map of the Merrimack estuary and surrounding shelf bathymetry is presented in Section 3.2 with the description of the realistic model used in this study.

There are several fresh water sources upcoast of the river that affect the ambient current near the Merrimack (see Section 1.2.3.1). Cape Ann is located $\sim$20 km southeast of the river mouth, constraining fresh water at times of high discharge. Plum Island, a barrier island, spans the coastal area between the Merrimack and

Cape Ann, behind which a tidal marsh with several minor fresh water inputs is located.

1.2.1 The Merrimack River estuary

The Merrimack River estuary is a highly time dependent salt wedge system (Geyer et al., 2008). Tidal and river forcing are strong and baroclinic circulation is weak; during high discharge the estuary is short and has a short memory that reflects the current forcing, as stratification is mixed away every tide by the strong tidal velocity and shallow bathymetry (Ralston et al., 2010b). Most mixing in the estuary happens due to internal shear early in ebb, and then in the bottom boundary layer later in ebb when the pycnocline thickens and deepens, interacting with the bottom. Tidal pumping induced by asymmetry in the halocline thickness and height and shear structure are much larger than the residual up-estuary salt flux (Ralston et al., 2010a; Chen et al., 2012). Tidal intrusion fronts, full water column fluxes of oceanic water into the estuary, occur during low/medium discharge at the Merrimack estuary mouth during flood tides (Largier, 1992), and later affect the salinity of water released over ebb. For discharges greater than 300 $\mathrm{m^3\ s^{-1}}$, fresh water is present at the river mouth during max ebb (Hetland and MacDonald, 2008; Ralston et al., 2010a), and at discharges greater than 400 $\mathrm{m^3\ s^{-1}}$, the salt wedge is pushed out of the mouth and most mixing of fresh water in the Merrimack estuary-plume system happens in the plume (Ralston et al., 2010b).

1.2.2 The Merrimack near-field

The near-field of the Merrimack River plume has been thoroughly studied from models and observations (MacDonald et al., 2007; Hetland and MacDonald, 2008; Chen et al., 2009). The Merrimack estuary mouth is narrow; ~ 280 m wide and man-made by jetties that concentrate the river outflow to deepen the ship channel and protect the estuary from harsh ocean conditions. A sand bar ∼5 m deep is located ∼300 m offshore from the mouth where the plume detatches from the bottom at max ebb. Discharge and tides, described in Section 1.2.2.1 and Section 1.2.2.2, force the near-field plume, affecting spreading and mixing near the river mouth.

1.2.2.1 River discharge

River discharge is a key forcing for the estuary and near-field; discharge affects the length of the estuary which is linked to buoyancy and momentum flux at the mouth and thus the evolution of the near-field through the length scales presented in Section 1.1.2. Estuarine and plume structure change with discharge; it affects where the majority of mixing in the estuary-plume systems happens. Because the Merrimack is tidally pulsed, several plumes from previous tides remain on the shelf and stratify ambient waters subject to the wind. Therefore past discharge patters (over the previous week or so) impact the development of a new tidal plume and its transition to a mid-field plume through the ambient salinity structure.

Merrimack River discharge is measured in Lowell, MA, ∼60 km up estuary from the mouth, and daily mean flow data during springs since 2006 is presented in the bottom panel of Fig. 1.3. The average discharge of the Merrimack is ∼600 $\mathrm{m}^3\ \mathrm{s}^{-1}$ with a minimum discharge of ∼100 $\mathrm{m}^3\ \mathrm{s}^{-1}$ in the summer (not shown) and peak discharge during spring freshet, when snowmelt from the surrounding mountains enters the watershed. During flood events, discharge reaches over 2000 $\mathrm{m}^3\ \mathrm{s}^{-1}$, as seen in April and Mays in 2006 and 2007; these peaks are due to storms that last several days. The flood peaks in discharge diminish significantly within 2-3 days and discharge returns to normal after about 2 weeks. The stars on the plot indicate times of field work where the near-field was measured during high (May 2006) and low-medium (April 2007) discharge; this data is presented in Chapter 2 and compared to model output.

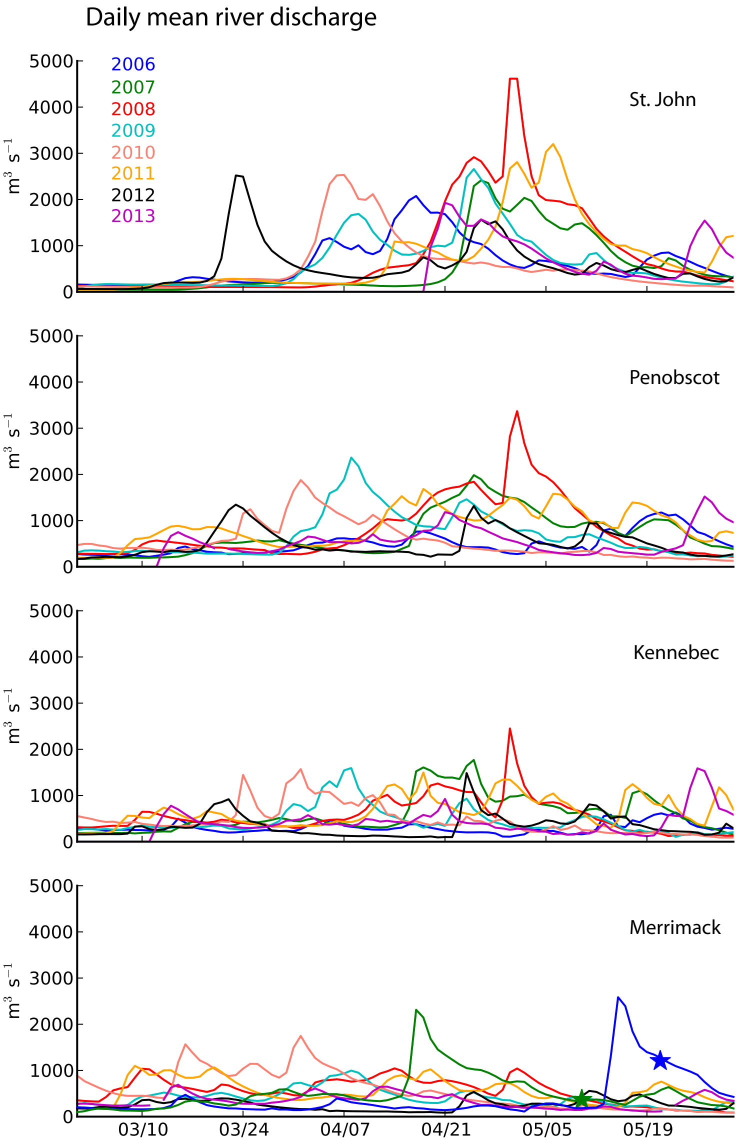

Figure 1.3: River discharge during springs from 2006-2013 for four major rivers in the Gulf of Maine. Data collected at USGS sites 01010500 (St. John), 01036390 (Penobscot), 01049265 (Kennebec) and 01070002 (Merrimack). Stars indicate times of field efforts in the Merrimack River plume.

1.2.2.2 Tides

In the salt wedge estuary, predominantly tidal forcing drives the circulation, and the consequence of the tide is transferred to the plume. The semidiurnal tide at the mouth of the Merrimack is $\sim$0.75 - 1.5 m. Tides are unmixed; the diurnal, spring/neap signals etc. are small relative to the semidiurnal. Tides contribute to the discharge at the mouth; Hetland and MacDonald (2008) estimate a 1 m tide results in 1800 m^3 s^{-1} tidal discharge at the mouth.

The tidal plume front is observed outside the estuary approximately 2 hrs after high water, but the model used in this research indicates the front is visible about 30 minutes before high water (referenced to the sea surface at the estuary mouth); this is likely because the observed sea surface height time series at the mouth of the Merrimack is forced at the boundaries in the model. In the model, the maximum tidal discharge occurs at $\sim$4 hours after high water, indicating a nearly standing wave. The ebb discharge lasts longer than the drop in sea surface height from high to low water by several hours, indicating a flood dominant estuary (Dyer, 1997) and a long-lived near-field plume.

During average discharge ($\sim$300 - 500 m^3 s^{-1}), the surface salinity at the mouth is fresh during max ebb (Hetland and MacDonald, 2008), however the mean salinity of the inflow is saltier later in ebb because of mixed water leaving the estuary full water column. During early ebb, the discharge at the mouth is a thin, fresh layer, and during flood the tide reverses full water column, bringing salty water into the estuary; this variability over a tidal cycle doesn't occur if river discharge is extremely high, in which case tidal pulsing is secondary and a more permanent near-field plume develops, as a huge quantity of fresh water is discharged throughout the tide.

1.2.2.3 Variability, structure and dynamics

Hetland and MacDonald (2008) show that plume properties in the near-field of the Merrimack, such as mixing and spreading rates, are a function of radial distance from the mouth, uniform along a plume ark, and that local and global spreading rates are proportional to the local gravity wave speed. After 2 hrs after high water, the steady approximation holds for several hours in the near-field, as local spreading estimates within the core of the plume begin to follow a linear offshore decay behind the propagating front. Chen et al. (2009) provide lateral spreading estimates of the Merrimack near-field plume from drifter observations that agree well with spreading estimates from a numerical model. They also show that the lateral momentum balance applied to flow perpendicular to a streamline indicates that at plume arks less than 1 km away form the mouth, the centrifugal force term is balanced by coriolis, buoyancy and interfacial stress, the latter two of which are correlated to mixing, while at arcs further form the mouth the momentum balance is primarily dominated by Coriolis and viscous stress is minimal. MacDonald et al. (2007) calculates dissipation rates in the Merrimack near-field plume form a control volume method and turbulence measurements collected by sensors mounted on a T-REMUS AUV to show that small scale heterogeneity present as localized bursts of turbulence dominate near-field mixing, and feedback between mixing and spreading is clear in the turbulent field. Local mixing rates in the Merrimack plume compare favorably with observations in other near-field plumes.

1.2.3 Offshore mid-field forcings

Ambient forcings characterize the shelf waters that the plume meets. As mentioned in Section 1.1.4.3, ambient currents, tides and wind not only affect the plume locally through its transition to the mid-field, but they also affect the regional circulation in the Gulf of Maine that feeds back into the shelf circulation in the vicinity of the Merrimack. In this section a picture of the general circulation in the Gulf of Maine is presented, with an emphasis on the wind, an important forcing for the Merrimack plume.

1.2.3.1 Ambient circulation in the Gulf of Maine

The Gulf of Maine is shaped by an indentation in the coastline ∼600 km long in the alongshore direction ranging from Nova Scotia, Canada, to Cape Cod, MA, and bounded by submarine banks ∼400 km offshore (Brooks, 1985). The mean interior surface circulation is an aticlockwise gyre, the northwestern leg of which is formed by density driven coastal flows due to river runoff and surface heating and cooling (Bigelow, 1927; Brooks, 1985). Several water masses are formed and modified on a seasonal cycle in the gulf, as convection in the basin's surface-to-mid water column occurs in the winter, restratification occurs in the summer, and tidal mixing occurs over the outer banks nearly year round (Bumpus and Lauzier, 1965; Brown and Beardsley, 1978; Brooks, 1985, 1994).

Six major rivers flow into the gulf. The top panels of Fig. 1.3 shows the monthly mean discharge of three key rivers that empty into the Gulf of Maine. The St. John River flows into the Bay of Fundy, and is the largest discharge river in the gulf, responsible for much of the buoyancy driven circulation. The Kennebec and Penobscot are smaller rivers; ∼150 km and 225 km upcoast from the Merrimack respectively. Similar discharge patterns and peaks are present in all three rivers, but they are most substantial in the time series of the St. John River. The Merrimack watershed appears to be unrelated to the discharge of the other three rivers shown, as the hydrographs are uncorrelated.

There are two coastal current systems in the gulf: the Eastern and Western Maine coastal currents, separated in the vicinity of Penobscot Bay where the Eastern Maine coastal current, transporting the majority of fresh water in the northeast gulf from the St. John River, is redirected offshore at times of low discharge; at high discharge the current continues downcoast to feed the Western Maine coastal current, which flows southwestward around the perimeter of south Maine, New Hampshire and Massachusetts. The Western Maine coastal current, fed by the Penobscot and Kennebec Rivers, is the coastal current that interacts with the Merrimack plume. The Western Maine coastal current is about 2 g kg^{-1} below the ambient salinity and $\sim$0.2 m s^{-1} during spring freshet; transport is closely related to the seasonal fluctuation in river discharge, but also varies on shorter time scales because of differential wind stress. Fresh water transport is significantly diminished between Cape Porpoise (near Penobscot bay) and Cape Ann, possibly due to offshore 'leakage' of fresh water or a change in the downcoast barotropic flow (Geyer et al., 2004).

1.2.3.2 Local and regional wind

Wind stress over the gulf in the summer is primarily from the southeast and in the winter is primarily from the northwest (Brown, 1998). Wind stress in the winter is about five times more energetic than in the summer, and the most energetic stress is found near the coast, south of Penobscot Bay; energetic winds are concentrated in the 2 - 10 day weatherband and diminish towards Isle of Shoals (Brown, 1998).

The Merrimack plume is strongly influenced by wind stress; at low-medium discharge, the affect of the wind extends close to the source (G. Kakoulaki, personal communication). Upcoast wind pulls the plume offshore and thins it, while downcoast wind traps the plume to the coast and thickens it (Fong and Geyer, 2001, 2002; Garcia Berdeal et al., 2002; Whitney and Garvine, 2005; Hetland, 2005; Choi and Wilkin, 2007). Far-field plumes are moved and mixed on the shelf to set the stratification of receiving shelf waters for the new tidal plume, so the wind stress over several days has a long-term effect (Hetland, 2005).

1.3 Scientific questions and hypotheses

1.3.1 How much source water reaches a plume front?

The focus of this study is the mid-field plume; this is where flow is redirected from offshore to downcoast. In a tidally pulsed regime, a clear division between the old and new plume water, as well as the near- and far-field, is the tidal plume front; the propagation, relaxation and dissolution of the front plays a significant role in mid-field dynamics.

Recent studies tie frontal propagation to the timing and magnitude of estuarine discharge, and there is observational evidence of this connection. Secondary frontal structures have been observed to traverse the core of the plume to overtake the front in IR imagery, and drifters released at the source have been recovered in the front of the Merrimack River plume. These experiments aim to quantify how much source water (estuarine discharge released over a single ebb) interacts with the tidal plume front.

Kilcher and Nash (2010) assert that frontal propagation is related to the flux of estuarine discharge over a tide; when ebb begins the front moves offshore and when ebb ends the front stops. A simple kinematic spreading model is used to prove this mechanism, but the model does not incorporate the complicated near-field mixing and spreading relationship and its effect on the evolution of the plume density anomaly. Although the model explains the Columbia plume evolution, the communication between the mouth and the front is unclear; how the front instantaneously slows when discharge slackens and how information travels through the plume body is not well understood, and can't be addressed without a dynamic model. The ideas in Kilcher and Nash (2010) have motivated the numerical experiments in the first half of this dissertation.

The goal of the numerical experiments is to examine pathways of source water through the core of the plume, quantify the amount of source water versus entrained water that reaches the tidal plume front and determine when the connection between the source and the front is arrested during an ebb cycle in an effort to better understand the role of time dependent estuarine discharge in sustaining frontal propagation. The importance of the front in mixing the total ebb discharge is also evaluated. These experiments are described in Chapter 3.

Hypothesis I: The interaction between the tidal plume source and front is arrested early in ebb; during most of ebb, overtaking velocities at the frontal convergence are confined to a region following the front that does not extend to the mouth. Therefore, the time dependent ebb discharge does not significantly influence frontal propagation.

Hypothesis II: Only a small fraction of early ebb discharge reaches the front before the connection between the mouth and front is arrested. Therefore, the majority of mixing of the total ebb discharge does not occur in the front.

1.3.2 How much mixing happens in a near-field plume?

Previous studies indicate that shear stress at the plume base is the primary mechanism that slows a near-field plume to subcritical velocities. Therefore, the transition to the mid-field is related to net mixing in the near-field; a reflection of the magnitude of local mixing near the source and the extent of the spreading (ergo mixing) region. Local mixing rates in near-field plumes in response to estuarine outflow conditions are well established in literature, but net near-field mixing in response to wind, rotation and tides slowing and mixing the plume is unknown.

The numerical experiments described in the second half of this dissertation aim to investigate the importance of rotation in the transition to the mid-field.

High discharge increases plume shear, but it also strengthens stratification, possibly limiting mixing. At the same time, high discharge adds buoyancy that should intensify spreading and thus increase mixing. The link between local and net plume mixing is not well understood in the case of variable river discharge. Furthermore, how discharge rate and rotation covary to modify the total mixing in the near-field is complex; as the plume grows, rotation diverts the flow from offshore to downcoast; possibly limiting the spreading region.

Previous studies report how fresh water discharge modifies the plume density anomaly. Halverson and Pawlowicz (2008) and Hetland (2010) give contradicting trends based on ferry data from the Fraser River plume in B.C., Canada and idealized, irrotational 3-D hydrodynamic model results. The goal of these experiments is to show that rotation causes the inconsistency between the two studies; it arrests the plume's offshore expansion, limiting spreading and the total mixing in the near-field. These experiments are described in Chapter 4.

Hypothesis III: Rotation suppresses net plume mixing by reducing the spreading region. Net mixing will increase with discharge in irrotational plumes and decrease with discharge in the presence of rotation, explaining the results of previous studies.

2. NEAR-FIELD MODEL - DATA COMPARISON

2.1 Merrimack River Mixing and Divergence Experiment

The Merrimack River Mixing and Divergence Experiment (MeRMADE) is an NSF funded study from 2006 - 2008, investigating mixing and spreading in near-field River plumes. The focus of MeRMADE is better understanding the transformations of riverine water through the near-field Merrimack River plume. The project goals are to relate mixing and spreading within the supercritical outflow region and to quantify the dependence of near-field flow characteristics to estuarine outflow variables (D. MacDonald and R. Hetland, unpubl.). Field efforts were conducted in 2006 and 2007 to answer these objectives and coupled with realistic numerical model output. Although several analyses have been published using these data and the numerical model, only a comparison of near-field mixing rates, which agree well, has been performed. The visual inspection of plume structure from data and modeled fields presented in this chapter is qualitative; it is intended to be a descriptive first step towards a more rigorous comparison and is necessary to asses the models capability and limitations in answering the questions listed in Section 1.3.

2.2 Observations

Data are collected over several tidal cycles, concentrated during mid-late ebb. These data are described in detail in MacDonald et al. (2007); they are shipboard, high-sampling-frequency CTD tow-yow transects through the core of the plume. Some transects have better horizontal resolution than others; all data are interpolated to a grid with 40 m spacing in the offshore direction and 0.25 m in the vertical. For some transects, the interpolation method occasionally produces small, fictitious wavelike patterns at the pycnocline; several interpolation schemes were tested, and this linear method produces the best result. The model fields shown in this chapter are simulated with the model described in Section 3.2.

Fig. 2.1 shows wind direction and magnitude at Isle of Shoals during the field project (grey blocked time periods). The Isle of Shoals wind time series is collected at NOAA meteorological station IOSN3, ∼25 km northeast of the river mouth and is used to force the model domain-wide. The stars in Fig. 1.3 indicate Merrimack discharge during the field work.

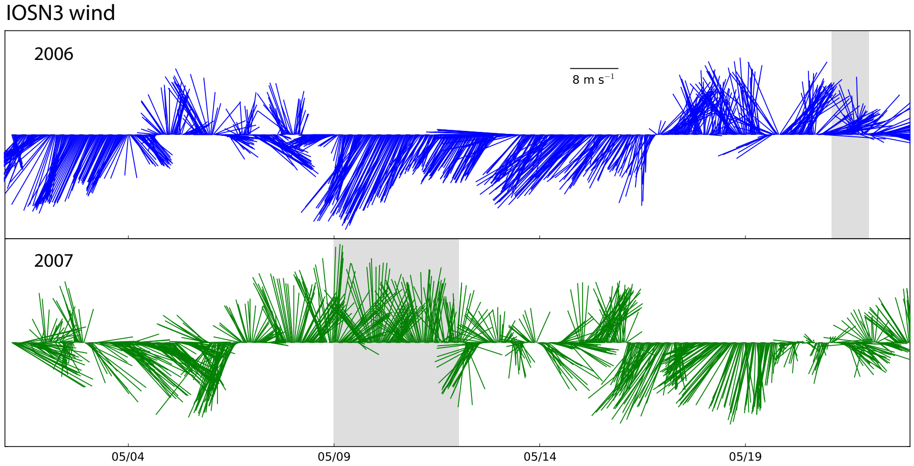

Figure 2.1: Three hourly wind during 2006/2007 field studies at NOAA NDBC station IOSN3 (Isle of shoals) located 25 km northeast of the Merrimack estuary mouth.

2.3 Comparison of 2006-2007 near-field data and model

A qualitative comparison of data collected in springs of 2006 and 2007 with the model used in the present study is presented in this section. At high discharge the model compares well with observations, but there are some small discrepancies. The upper left panel of Fig. 2.2 shows a transect during the high discharge period in May 2006 at late ebb; the upper panel shows the data and the lower panel shows the model.

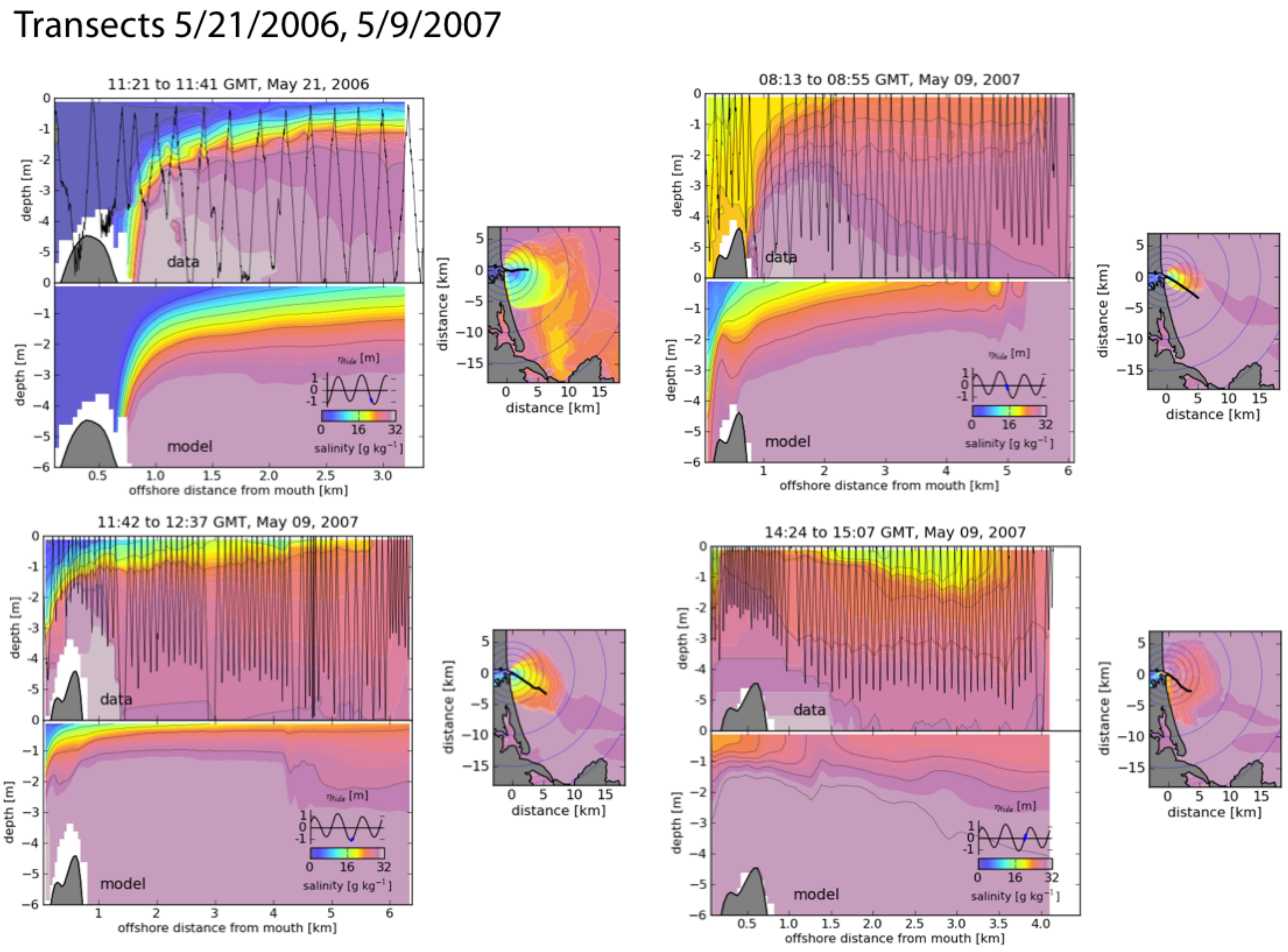

Figure 2.2: Four transects through the plume core on 5/21/2006 and 5/9/2007 from the model (bottom panels) and observations (top panels). Black lines in the data panels show the CTD position. Location of the transect and modeled surface salinity during the transect is shown in the right panels.

The lift off point is consistent between the model and the data, but offshore, the observations illustrate a slightly thinner pycnocline and deepening in near-ambient isohalines. MacDonald et al. (2007) shows that interfacial mixing rates in the near-field between the model and observations, calculated from a control volume approach, compare favorably, but perhaps the thick pycnocline is a result of misrepresented surface stress in the model (possible, since a domain-wide wind forcing is used), although the impact of wind is minimal near the river mouth. It is also possible that the core of the near-field is offset between the model and data; this could occur because of domain-uniform wind forcing or because the ambient stratification and shelf currents are not realistically modeled without exchange with the gulf at the boundaries. Radial transects measured 1 km from the river mouth (not shown) indicate that the core position is not offset significantly in the model, but even a small offset will cause the observed stratification data to be quite different from the model.

The remaining panels of Fig. 2.2 show a time sequence of transects during the low discharge field effort in May 2007. Fig. 2.3 similarly shows a time sequence during another tide at low discharge in May 2007. The model compares to the data best at late ebb (bottom-left panels); the lift off location is similar, but the plume is slightly saltier and thinner in the model. The model performs poorly during flood (bottom-right panels), but this is expected because the plume velocities are small and the ambient circulation and wind, which is only semi-realistic in this model, affects the advection of the plume more. At mid-ebb, the model and data are most dissimilar, with the liftoff further offshore at the bar and a more thoroughly mixed ebb discharge revealed in the data; this is visible in the upper right panels of Fig. 2.2 and Fig. 2.3. This could be an artifact of insufficient estuarine mixing in the model; mixing in the bottom boundary layer becomes important later in ebb in the estuary

(Ralston et al., 2010a), and over the bar, bottom mixing is important as well, but this study focuses on interfacial mixing, so bottom stress is under-developed in the model. Furthermore, if the modeled stratification of the inflow is corrected in the estuary to match the data (made saltier), then it would perhaps stay attached to the bottom further offshore and lift of at the bar as seen in the data.

A thin plume is highly susceptible to advection and mixing by wind. In 2007 the discharge was low and southerly wind forcing high; this scenario created a plume pushed offshore/upcoast and thinned, which is likely the most difficult type of plume to model in the current setup, with a goal of matching the measured plume. The salinity of mid-ebb water leaving the estuary is a problem solved by addressing estuarine mixing. Ralston et al. (2010a) reports several constraints on mixing adapted in an unstructured grid model in order to preserve the time-dependent stratification in the salt wedge; it is not simple and beyond the scope of this project. Currently, the model is run semi-realistically, and intended to study near-field mixing on a single-ebb basis; no interaction between ebbs is considered and the parameters at the inflow is the important, driving factor for the plume, not the reality of the estuarine mixing. Furthermore, previous studies show that near-field plume mixing rates compare well between the model and observations (MacDonald et al., 2007). The scientific questions asked in this research are within the limits of the model and it does a reasonably good job recreating observations during late ebb, especially at high discharge.

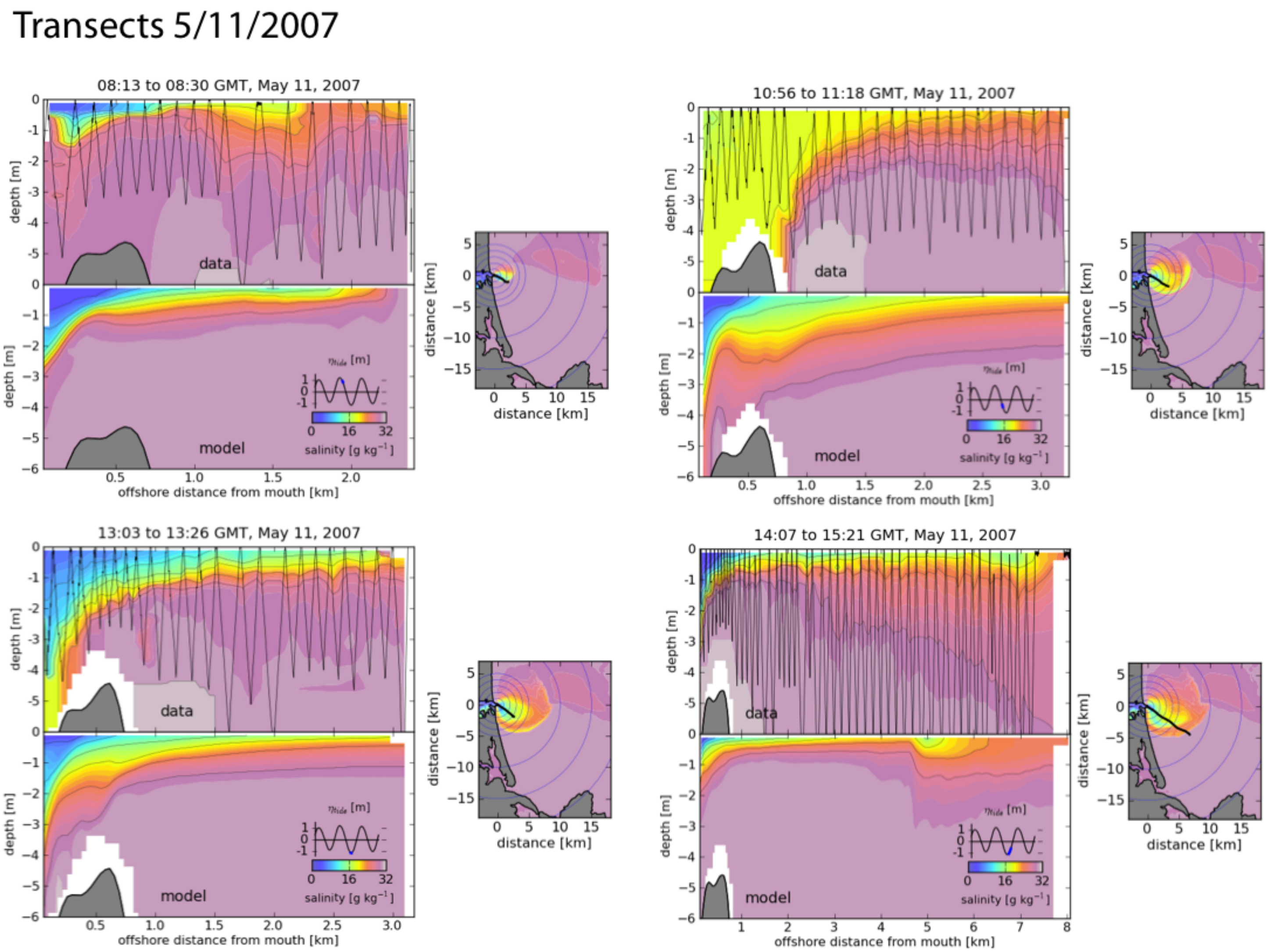

Figure 2.3: Four transects through the plume core on 5/11/2007 from the model (bottom panels) and observations (top panels). Black lines in the data panels show the CTD position. Location of the transect and modeled surface salinity during the transect is shown in the right panels.

3. RIVER PLUME SOURCE-FRONT CONNECTIVITY

3.1 Introduction

Temporal variability of fresh water discharge from estuaries is an important element of the physical environment that shapes coastal ecosystems. In tidally modulated regions, buoyant water of riverine origin is pulsed from an estuary mouth onto the shelf during the ebb tide. The buoyant water shoals and spreads over dense receiving shelf water, creating an energetic shear mixing region (Hetland and MacDonald, 2008). The plume spreads offshore as ebb progresses, and accumulations of nutrients, plankton and other materials may be trapped and transported in the seaward boundary of each ebb pulse by the strong convergence that exists there (Scotti and Pineda, 2007). The interaction between source water and ambient shelf water is amplified at the tidal plume front; recent studies show that in some estuary-shelf systems, the tidal plume front is where a large portion of source water mixing from fresh to ocean salinities takes place (Orton and Jay, 2005; Pritchard and Huntley, 2006).

In plumes that discharge from narrow estuaries (i.e. a mouth width smaller than the internal deformation radius), the ebb discharge spreads offshore behind a front that propagates as a gravity current (Garvine, 1987; Orton and Jay, 2005). Communication between the mouth and the front is achieved through source water traversing the plume and overtaking the front (Garvine and Monk, 1974; O'Donnell et al., 1998; Marmorino and Trump, 2000). Previous laboratory studies of gravity currents and observational studies of buoyant plumes show that fresh water leaves the source, travels through the core of the plume and is cycled through the front; this supply of buoyant water to the front is necessary to sustain frontal propagation throughout ebb. A wealth of studies focus on dynamics in the plume core (MacDonald et al., 2007; Hetland and MacDonald, 2008) and the structure of the plume front (Marmorino and Trump, 2000; Orton and Jay, 2005; Jay et al., 2009), but few studies examine the connection between both regions. Linking all plume regions is necessary to understand plume evolution (McCabe et al., 2008), yet the numerical models described in Garvine (1982, 1984, 1987), O'Donnell (1990) and Hetland (2010) focus on the effect of inflow variables on plume interior mixing to determine expansion; the details of frontal dynamics are overlooked. Alternatively, Jay et al. (2010) assume that local frontal dynamics are responsible for the advancement of the plume in a numerical study of tidal plume expansion. Some observational studies, such as Luketina and Imberger (1987) and Kilcher and Nash (2010), link ebb discharge at the estuary mouth to frontal propagation, presenting a nearly complete picture of tidal plume evolution, however, they do not examine the path of source water through the plume core in detail. Processes at the source, the near-field and the front influence plume propagation, but the relative importance of each region (or forcing offshore) in determining the advancement of the tidal plume front is unclear. The relationship between the time dependent estuarine discharge and frontal propagation is examined in this study using a kinematic approach; how the estuarine outflow rate and the dilution of water through the plume interior govern the amount of source water to reach the front, and thereby its propagation offshore, is evaluated.

The propagating front has a convective, bore-like head structure, and in the presence of rotation, a trailing zone of strong along-front velocity shear (Garvine and Monk, 1974; O'Donnell et al., 1998; Marmorino and Trump, 2000). Britter and Simpson (1978) identify strong mixing and entrainment in lee of the front as the surface plume propagates behind it. Oncoming plume water flows into the frontal head, creating a convergence zone of overtaking velocities in the direction of front propagation where mixing between plume and ambient water takes place (Marmorino and Trump, 2000). Luketina and Imberger (1987) measure a Richardson number consistent with turbulent mixing up to 300 m behind the front in Koombana Bay, Austrailia and Orton and Jay (2005) show that the 100 m of plume area behind the front is responsible for 20 % of tidal plume mixing in the Columbia River plume. Pritchard and Huntley (2006) measure stronger mixing at the front than wind and interfacial mixing in a small plume in the English Channel; strong enough that a plume doesn't form 65 % of the time during spring tides because the plume water is mixed through the front during its early formation. Previous studies support strong mixing in the frontal region, however, there are many processes that dilute a parcel of source water as it translates the plume as well; a key factor is the increasing plume surface area over ebb that source water traverses; a scale governed by the front position. An aim of this study is to quantify the amount of source water that interacts with the front over a single ebb pulse. This information has been overlooked in previous studies that evaluate total plume mixing at the front simply from mixing measurements at the front relative to the fresh water flux at the source; a large portion of buoyant water mixed at the front could be entrained from older plumes, and furthermore, much source water released during the current ebb pulse may not interact with the front at all.

3.2 Model and methods

In this study, realistic and idealized numerical simulations of the Merrimack River estuary-shelf system are used to study river plume source-front connectivity. The Merrimack is a medium discharge, east coast river (typically 300 - 700 $m^3\ s^{-1}$) and a $\sim$ 1.5 m semidiurnal tide pulses the discharge at the estuary mouth. The Merrimack is an ideal location to study classic plume properties because of its relatively straightforward dynamics, which are largely due to the narrow estuary, uncomplicated geometry of the mouth and coast, and shelf bathymetry.

The Regional Ocean Modeling System (ROMS, version 3.5) (Shchepetkin and McWilliams, 2005), a hydrostatic, sigma-coordinate model, is paired with a curvilinear grid that represents the Merrimack River estuary and shelf region on the Massachusettes/New Hampshire border of the US east coast. Fig. 3.1 shows the model domain. The grid spans the head of the Merrimack estuary to ∼20 km offshore, and ranges from ∼10 km upcoast of the mouth to Cape Ann, ∼20 km downcoast of the mouth. The domain adequately contains the plume under most realistic wind and ambient current regimes.

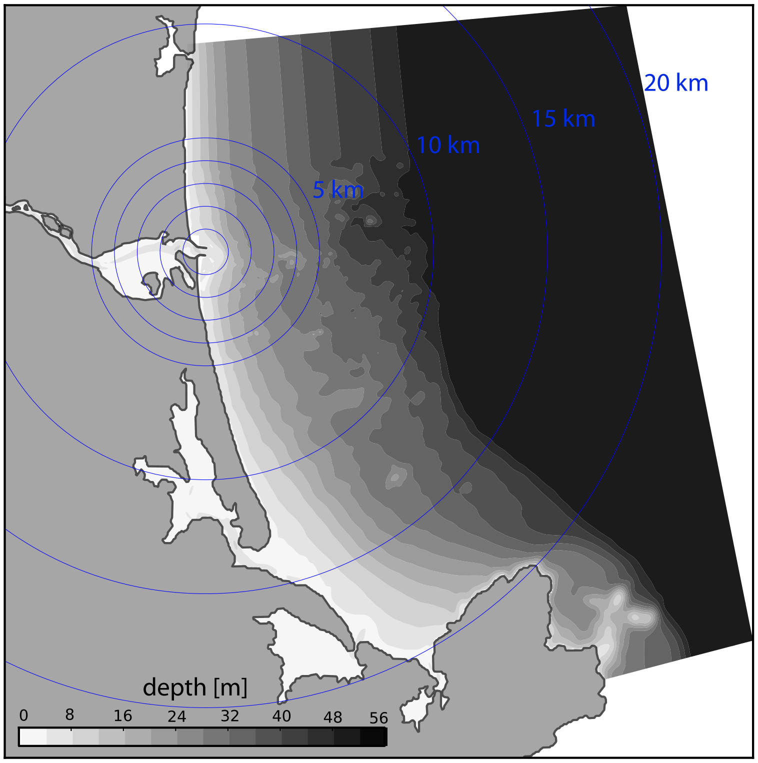

Figure 3.1: Merrimack River estuary and shelf domain. Grid spans approximately 10 km up the estuary from the mouth to 20 km offshore into the Gulf of Maine. Grid spacing is 40 m at the estuary mouth and 100 m at the offshore boundary.

There are 30 vertical layers and the spatial resolution ranges from ~40 m at the mouth to ~100 m at the offshore boundaries. The width and average depth at the mouth is 276 m and 6.3 m respectively and the model bathymetry includes a shallow bar ~300 m seaward of the estuary mouth where fresh water loses contact with the bottom during plume formation. Fresh water enters the domain through a wall 10 km up river from the estuary mouth. It generally takes less than 12 hours for a parcel of water to travel the length of the estuary and enter the coastal ocean.

MPDATA vertical and horizontal tracer advection (Smolarkiewicz and Clark, 1986) is implemented. Tracers are horizontally mixed along geopotential surfaces. Vertical mixing is described by k-ϵ turbulence closure coupled with Canuto A-stability function formulation (Canuto et al., 2001). Horizontal smoothing of buoyancy and shear is implemented. Quadratic bottom friction is incorporated into the momentum equation and conservative, parabolic spline reconstruction is used for vertical derivatives in the model. A Flather boundary condition (Flather, 1976) is used for 2-D velocity components and the free surface and an Orlanski boundary condition is used for 3-D velocity components and tracers at the north, east, and south open boundaries (Orlanski, 1976).

For realistic simulations, domain wide wind forcing is implemented from a NOAA meteorological station at the Isle of Shoals, approximately 25 km northeast of the estuary mouth. Wind data is 3 hr decimated. The wind is removed in some idealized cases to study the front. River discharge implemented in the model is recorded by the USGS at a hydrologic unit at Lowell, MA. A southward flowing ambient coastal current (~5 cm s^{-1}) is applied at the northern open boundary. The semidiurnal tide is forced at the open boundaries by the free surface. In these experiments, the tidal phase is referenced to the sea surface height at the estuary mouth. Ebb generally begins before high water and tides are longer than six hours in the simulations.

Modeled physical parameters at the river mouth over the April/May 2011 simulation are presented in Fig. 3.2. Gray regions highlight tidal cycles analyzed in this research and Fig. 3.3 shows surface salinity every ~ 0.5 hrs over the indicated tides.

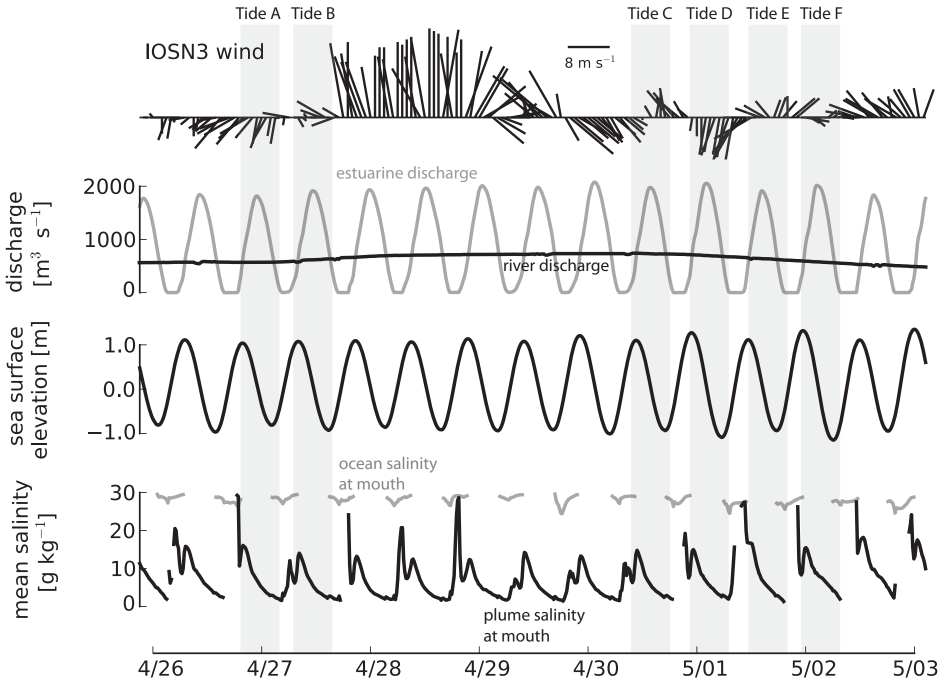

Figure 3.2: Top panel shows NOAA Isle of Shoals wind during the April/May 2011 simulation. Middle panels show river inflow into the domain, estuarine discharge into the ocean part of the domain and sea surface elevation at a grid cell at the river mouth. Bottom panel shows the mean salinity at the river mouth of inflowing (plume) and outflowing (ocean) water into the ocean part of the domain. Shaded times indicate ebbs analyzed in this research.

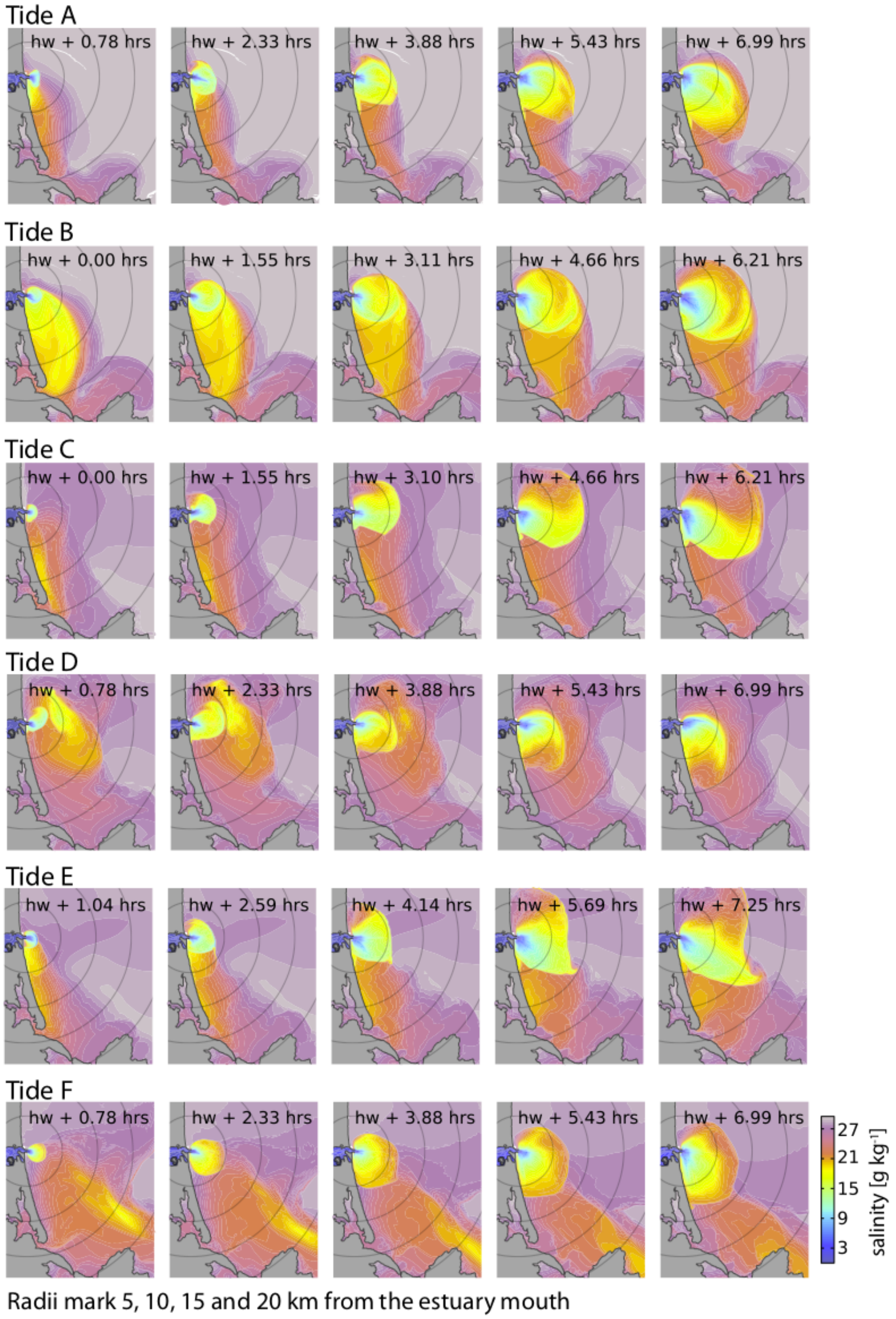

Figure 3.3: Time sequences of sea surface salinity over the ebbs highlighted in Fig. 3.2.

The tidal plume front is tracked by 1000 surface drifters released in an arc behind the front when it first emerges from the estuary mouth (this generally happens before high water throughout the simulation). The drifters follow the front as the plume spreads offshore. Fig. 3.4 illustrates the drifter trajectories ∼hourly over ebb (and into early flood) during the six tides highlighted in the previous figures. Since the drifters spread apart as time passes, the front is linearly interpolated where the distance between drifters is more than 300 m. The mean wind direction and magnitude over the ebb cycle (3 hourly from NOAA IOSN3 station) is displayed with the arrow on the upper right corner of the panels in Fig. 3.4. River discharge ranges from 500 to 700 $m^3\ s^{-1}$ between the tides.

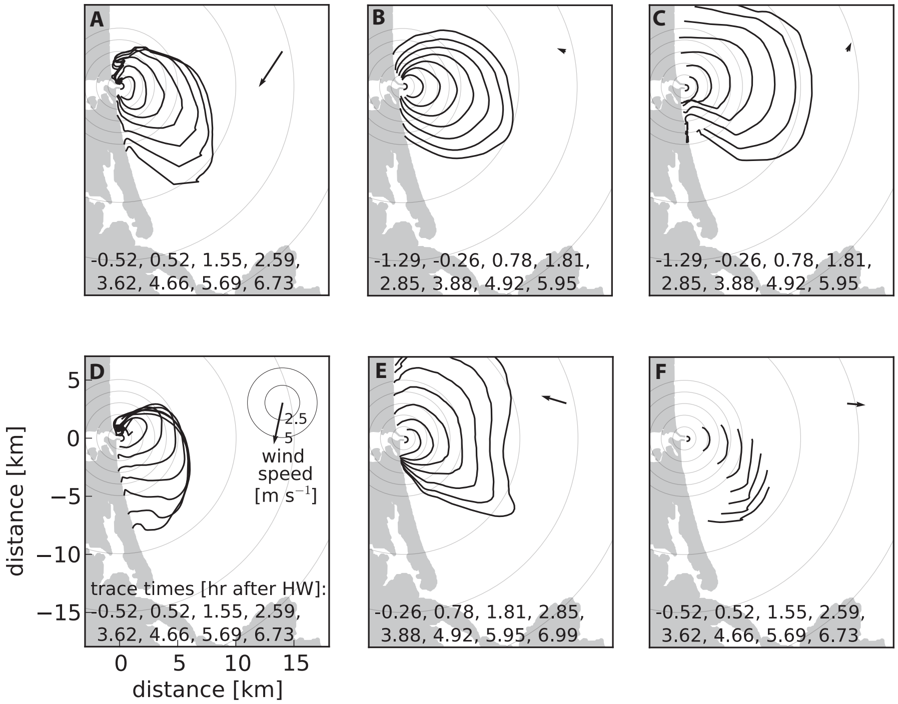

Figure 3.4: Evolution of the front during ebbs highlighted in Fig. 3.2. The front is defined from numerical surface drifters released at the start of ebb behind the front and marked by the black lines. Trace times are relative to high water at the estuary mouth. Arrows represent the mean wind direction and magnitude over ebb.

Fig. 3.5 shows surface convergence at four times during an ebb pulse (tide A in Fig. 3.2). The numerous fronts and wave like convergences interact throughout the simulation, creating a dynamically rich ambient field to receive the new tidal plume.

The red line marks the front location from surface drifters released at the mouth at the beginning of ebb. The front marked by the drifters follows the primary front shown in the surface convergence during ebb, and therefore validates that numerical surface drifters provide a reasonable estimate of the location of the tidal plume front.

Source water pathways are investigated using surface drifter clusters and passive dye tracer released at the estuary mouth during tides A, C and E. Since the drifters only follow surface advection, dye is released full water column at the mouth to study the affect of vertical mixing on source water traversing the plume. When dye is released, the tracer concentration is initialized to one at the river mouth and diminishes as the dye mixes with ocean water; cells with no dye have a tracer concentration of zero. The first ∼15 min of ebb are not tagged with dye because of of the time gap between saving simulation data, so 'total' source water calculations are missing this volume. The dye experiments analyzed in this research are listed in Table 3.1. Clusters of 50 surface drifters are released with dye. Simulations indicate that the dye generally follows the drifters; dye spreads more than the drifters, but reaches the front at approximately the same time.

A wall is added to the grid at the estuary mouth at mid-ebb in the gate experiments described in Table 3.1, damming estuarine discharge. Idealized cases of tide A are analyzed with the gate; idealized wind forcing is used to eliminate the wind driven advection of the front. Wind is damped to zero during the flood previous to tide A so that the ambient stratification is not changed significantly. Without wind forcing, the plume evolves differently than the plume in Fig. 3.4, panel A. These experiments provide a way to investigate the response of the front when no source water is supplied to it and directly test the idea that ebb discharge drives the frontal propagation and relaxation offshore.

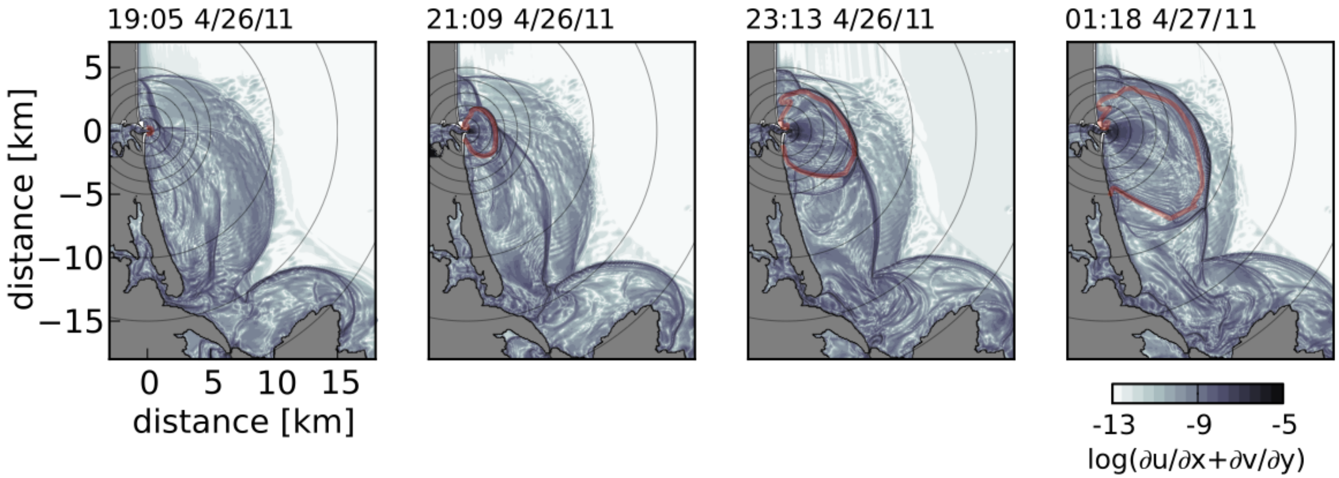

Figure 3.5: Evolution of tide A labeled in Fig. 3.2. Panels are approximately two hours apart. Blue contours show log of surface convergence. The red line identifies the location of the front from numerical surface drifters.

Table 3.1: Dye release experiments during the April-May 2011 Merrimack River plume simulation. All dyes are released full water column at grid cells spaced 40 m apart across the estuary mouth (at the end of the jetties). 'Start of ebb' is the time step (relative to high water) when the tidal plume front emerges from the estuary mouth and drifters are released to mark the front position.

Experiment	Tide	Start of ebb	Start of release	No. dyes released	Release frequency	Release duration	Dam closing time
A1	2nd ebb, 4/26/11	- 0.52 hrs	- 0.52 hrs	1	throughout ebb	6 hrs	—
C1	1st ebb, 4/30/11	- 1.29 hrs	- 1.29 hrs	1	throughout ebb	6 hrs	—
E1	1st ebb, 5/1/11	- 0.26 hrs	- 0.26 hrs	1	throughout ebb	6 hrs	—
A3	2nd ebb, 4/26/11	- 0.52 hrs	+ 0.00 hrs	3	every 2 hrs	1 hr	—
C3	1st ebb, 4/30/11	- 1.29 hrs	- 0.77 hrs	3	every 2 hrs	1 hr	—
E3	1st ebb, 5/1/11	- 0.26 hrs	+ 0.27 hrs	3	every 2 hrs	1 hr	—
A12	2nd ebb, 4/26/11	- 0.52 hrs	- 0.52 hrs	12	every 30 min	30 min	—
Gate0*	2nd ebb, 4/26/11	- 0.52 hrs	- 0.52 hrs	1	throughout ebb	6 hrs	—
Gate1a*	2nd ebb, 4/26/11	- 0.52 hrs	- 0.52 hrs	1	during early ebb	1.3 hrs	—
Gate1b*	2nd ebb, 4/26/11	- 0.52 hrs	- 0.52 hrs	1	during early ebb	1.3 hrs	+ 0.78 hrs
Gate2a*	2nd ebb, 4/26/11	- 0.52 hrs	- 0.52 hrs	1	during early ebb	2.33 hrs	—
Gate2b*	2nd ebb, 4/26/11	- 0.52 hrs	- 0.52 hrs	1	during early ebb	2.33 hrs	+ 1.81 hrs
Gate3a*	2nd ebb, 4/26/11	- 0.52 hrs	- 0.52 hrs	1	during early ebb	3.37 hrs	—
Gate3b*	2nd ebb, 4/26/11	- 0.52 hrs	- 0.52 hrs	1	during early ebb	3.37 hrs	+ 2.85 hrs
Gate4a*	2nd ebb, 4/26/11	- 0.52 hrs	- 0.52 hrs	1	during early ebb	2.07 hrs	—
Gate4b*	2nd ebb, 4/26/11	- 0.52 hrs	- 0.52 hrs	1	during early ebb	2.07 hrs	+ 1.55 hrs

* Idealized wind forcing experiments

3.3 Results

3.3.1 Temporal variability of source water properties

Source water is advected and diluted within the plume body, affecting the quantity of new estuarine water that interacts with the front. In this section, the temporal and spatial variability of source water is examined as it travels trough the tidal plume. Surface dye concentrations and vertical structure over a cross-shore transect are given in Fig. 3.6 for tide A during mid-ebb (experiment A3). Surface concentrations display the accumulation of dye along the path of the ebb jet and the lateral spreading and accumulation of dye near the front. The panels showing the dye depth structure indicate that the tail of a dye patch moves slower than dye at the surface because of the sheared current structure in the plume.

Only the first few dyes released interact with the front during the evolving tidal plume stage. As ebb discharge wanes, a small portion of the second dye pulse (released ∼2.5 hrs after high water) has reached the front. The release two hours later does not reach the front until well into the following flood. It takes several hours for source water to travel through the plume as it grows, and the water released late in ebb doesn't reach the discharge front until the next ebb, near the entrance to Plum Island Sound.

Surface drifters released at the mouth indicate that source water-front interaction is limited spatially; the first set of drifters released ∼30 min after the start of ebb (not shown, released with the pink dye in Fig. 3.6) spreads radially and interacts with the front in all directions, but the subsequent drifter releases follow the core of the plume along the central axis and do not reach the upcoast and downcoast portion of the front. This behavior is explained by diminished lateral spreading associated with weak lateral density gradients as the plume body fills with fresh water. Increased jet inertia in the plume core related to high estuarine discharge later in ebb also contributes the the drifter behavior (max ebb occurs at ∼4 hrs after high water). These trends are consistent between tides A, C and E.

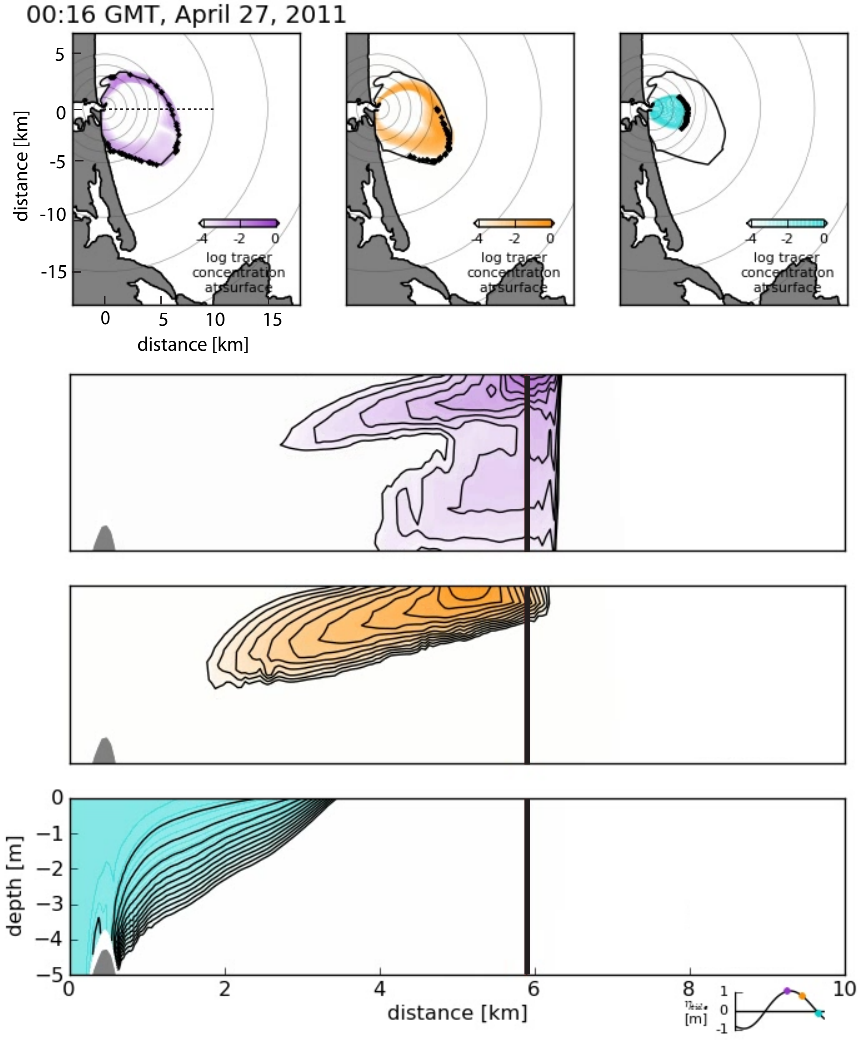

Figure 3.6: Surface concentration (top panels) and vertical structure (bottom panels) of dyes at max ebb (during tide A labeled in Fig. 3.2) that are released full water column at the estuary mouth. Dyes are released for an hour during ebb at times indicated by the matching colored dots on the sea surface height plot in the lower right. Vertical sections over an offshore transect marked by the dotted line in the upper left panel are displayed. Dye concentration is contoured on a log scale.

Dye releases are performed with higher temporal resolution in experiment A12 to better establish the release time of dyes that interact strongly with the tidal plume front. The upper four panels of Fig. 3.7 depict time series of dye concentration weighted mean plume properties for twelve dyes released in 30 min blocks over tide A. Dye weighted properties, *C(t)*, are calculated in the plume core defined by an angle from the mouth (15° to -50°) and are calculated by the volume integration

$$C(t) = \frac{\int dye(x,y,z,t)\phi(x,y,z,t)dV}{\int dye(x,y,z,t)dV}, \tag{3.1}$$

where x, y, z and t are east-west coordinate,north-south coordinate, vertical coordinate and time variables respectively. ϕ is a physical variable such as salinity, velocity, depth or distance from the mouth and *dye* is the river water concentration. The initial values of the dye-weighted time series indicate the tidally driven variability in inflow parameters. The estuarine outflow freshens, deepens and increases speed during early-mid ebb. The shoaling and accelerating as source water moves offshore after lift off is clear in the time series of the first few dyes released; the dyes slow and deepen because of plume mixing later in ebb.

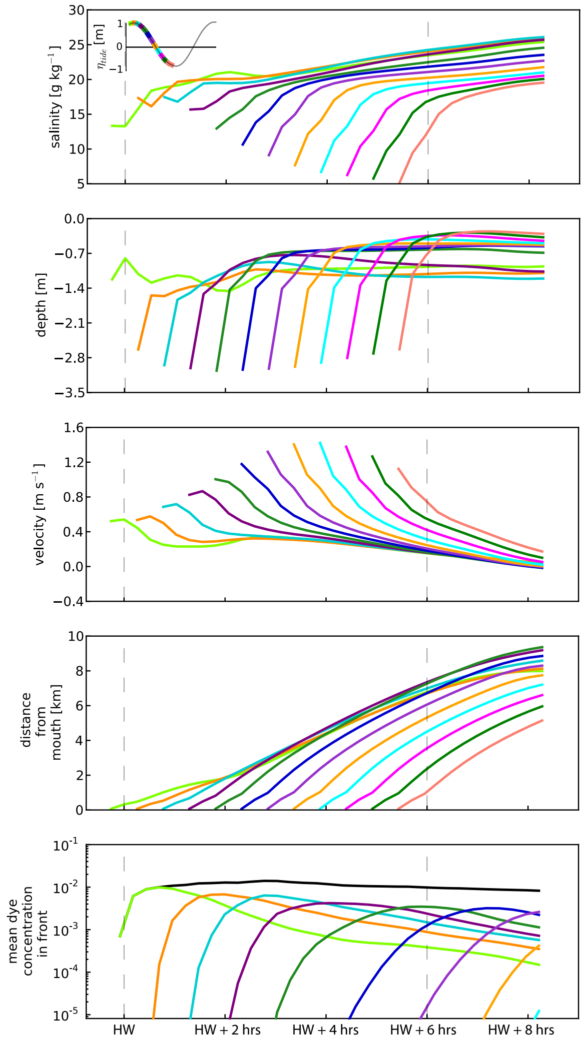

Figure 3.7: Top four panels show time series of dye concentration weighted mean plume properties during tide A. Dyes are released back-to-back for 30 minutes full water column at the estuary mouth during ebb at times indicated by the matching colored dots on the sea surface height plot inset in the top panel. The bottom panel displays mean dye concentration within the frontal zone defined over 600 m from the ocean side to the plume side of the front. The black line in the bottom panel indicates mean source water concentration in the frontal zone (tagged by a dye released throughout ebb). Calculations are made in the plume core defined by an angle from 15° to -50° offshore from the mouth.

3.3.2 Source water age in the plume front

The bottom panel of Fig. 3.7 shows mean dye concentration in the plume front defined over 600 m from the ocean side to the plume side of the front. Dye concentration in grid cells within a 300 m radius of the front defined by drifters are averaged. Mean dye concentration in the front, $C_{front}(t)$, is evaluated by

$$C_{front}(t) = \frac{\iiint\limits_{front} dye(x,y,z,t)dxdydz}{\iiint\limits_{front} dxdydz}. \tag{3.2}$$

The bottom panel of Fig. 3.7 indicates that dyes released late in ebb do not reach the front until nearly the beginning of the next ebb, and by this time the front is one of many discharge fronts in the far-field. Only source water released in the first few hours of ebb interacts with the front as it propagates offshore as a tidal plume. Although source water released after this time does not interact directly with the front, it still plays a role in plume evolution; this water sets the stratified initial condition on the shelf that the next plume meets.

The temporal evolution of dyes exhibiting maximum concentration in the front during tide A is given in the top panel of Fig. 3.8. The 30 min dye releases described in Fig. 3.7 (experiment A12) are used. This result further illustrates that only water released during early ebb interacts with the front. This information, combined with the distance of the front offshore (its mean position in the plume core), gives an estimate of the mean plume speed, or flushing rate of source water through the plume layer. The mean plume speed over ebb A is presented in the lower panel of Fig. 3.8 (black line). The gray line shows the mean estuarine discharge velocity at the mouth; the peak mean plume speed appears to be related to the high discharge velocity at max ebb (∼4 hrs after high water).

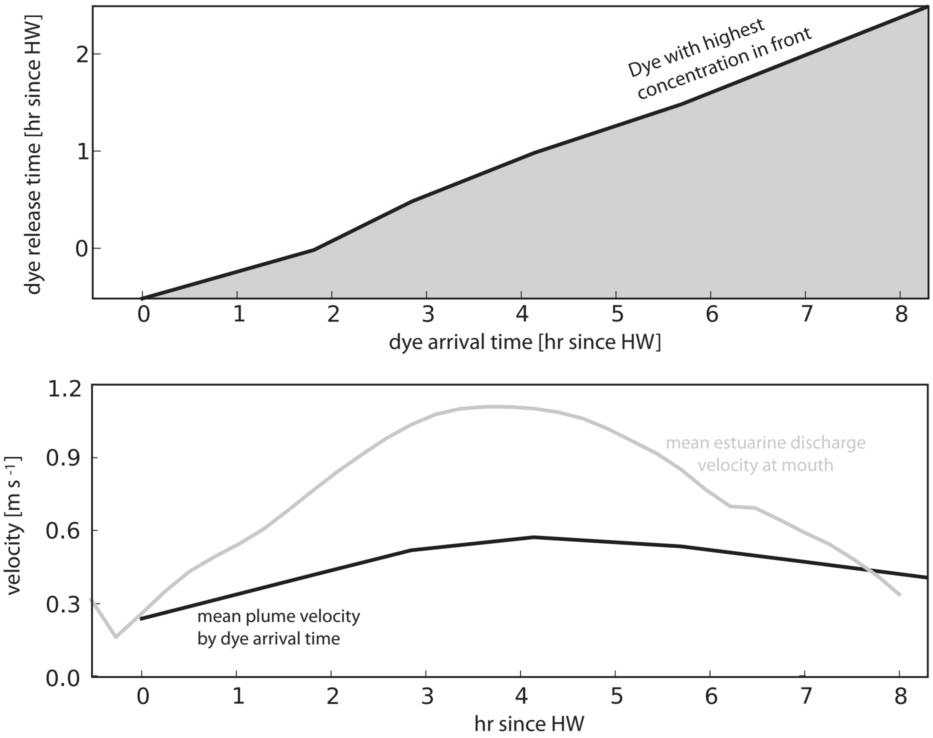

Figure 3.8: Top panel displays the temporal evolution of dyes with the highest concentration in the front plotted by their release time at the mouth and arrival time in the front. Gray shading indicates dyes that have reached the front but are no longer the primary dye present in the frontal zone, as they have been diluted by ocean water and new source water. The bottom panel illustrates the speed of source water though the plume by its arrival time in the front (black line) and the mean velocity of outflowing water at the estuary mouth (gray line). Estimates of mean dye concentration in the front and front distance offshore are calculated within the plume core from 15° to -50° offshore from the estuary mouth.

The time series indicate that although new source water replaces old source water in the front following an approximate linear trend, a parcel of source water arriving at the front around 4 hours into ebb moves fastest offshore on average. As the plume expands, wind, ambient flow and rotation are able to redirect the flow in the plume interior from the front. There is more variability in current speed and direction across the plume at mid-ebb because of these phenomena, but the inertia of the estuarine outflow is the principal driver of source water offshore; the fastest plume speeds are likely influenced by the timing of the maximum volume flux at the estuary mouth.

3.3.3 How much source water reaches the plume front?

The diluted state of source water when it reaches the front stems from interior plume mixing. Tide C (experiment C1) is analyzed in this section, with dye released throughout ebb to tag new plume water. This tide is chosen because the plume spreads more radially than other ebbs, and radial fluxes behind the front are easier to estimate.

The frontward flux of source water towards the front, $Q_{front}(t)$, is calculated by

$$Q_{front}(t) = \iint_{plume} u_{front}(\theta, z, t) dye(\theta, z, t) d\theta dz, \tag{3.3}$$

where u_{front} is the plume radial velocity in the front-following frame, dye is the source water concentration and θ is an angle from the mouth (an arc length is calculated for the radial flux).

The flux of source water overtaking the front is shown in the top panel of Fig. 3.9. Model velocities are rotated in the radial direction from the mouth. The plume is divided into 5° angles from the mouth and the mean radial velocity of the front within each angle is subtracted from the plume radial velocity field within each angle to investigate plume flow in the front-following frame. Average vertical profiles of velocity and source water concentration are used to calculate the radial flux 350 m behind the front. Plume velocity and source water concentration are averaged 300-400 m behind the front resulting in a mean vertical profile in each angle and the flux is calculated assuming an arc length from a circular spreading front. The center panel of Fig. 3.9 shows the estuarine discharge. The bottom panel of Fig. 3.9 shows the temporal evolution of the fraction of overtaking source water to the estuarine discharge. The source water flux behind the front in the top panel is traced back in time by the age relation (Fig. 3.8) and plotted as a precent of the past estuarine discharge. The result presented in Fig. 3.8 is from tide A, but analysis of different tides (not shown) suggest that the timing of source water reaching the front is approximately the same for all ebbs; the age relation in Fig. 3.8 is therefore applied to analyses of all tides.

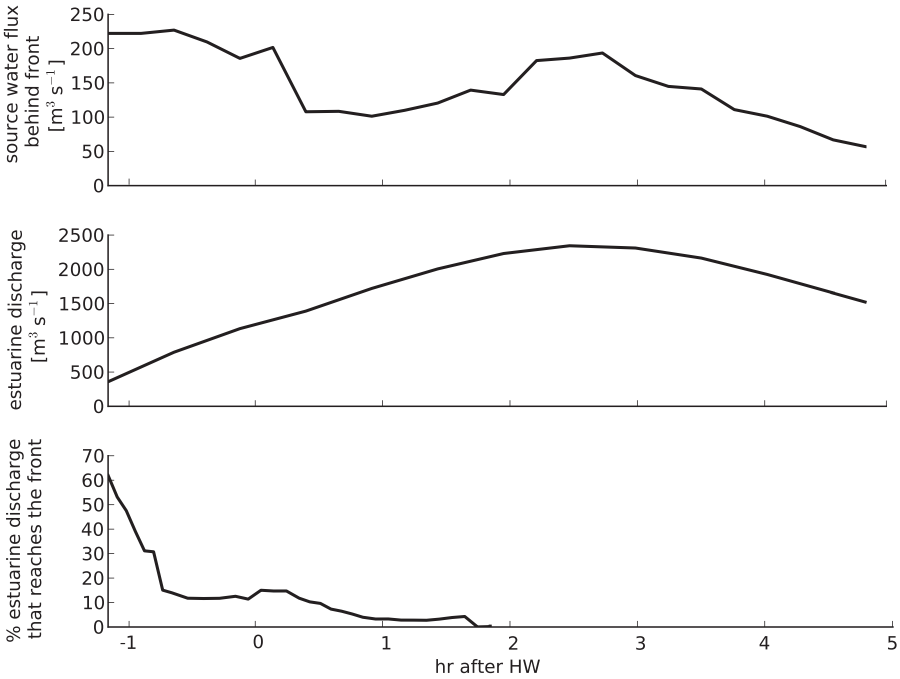

Figure 3.9: Top panel shows the flux of overtaking source water in the front following frame 300 m behind the front during tide C. Middle panel shows discharge at the estuary mouth during tide C. Bottom panel shows the percent of the estuarine discharge that overtakes the front by tracing the source water flux behind the front back in time via the age relation presented in Fig. 3.8.

The flux of source water behind the front is an order of magnitude smaller than the ebb discharge becasuse much of the ebbed water is mixed in the plume body. Early in ebb, a large percentage of source water overtakes the front; overtaking velocities span the entire plume early in its formation, but quickly diminish and exist only in the plume core, contributing to the small percentages throughout most of ebb. Also note that there is a slight increase in overtaking source water at the timing of max ebb at the mouth.

3.3.4 Frontal propagation without a supply of source water

The response of the tidal plume front when a dam at the estuary mouth is closed during ebb is now investigated. These experiments directly test the hypothesis that the time dependent estuarine discharge controls the frontal speed and relaxation offshore. Tide A is analyzed in this subsection, but wind forcing is eliminated to prevent the wind driven advection of the front. Without wind forcing, the plume evolves differently than tide A, but given the previous results, we assume the timing of source water translation through the plume is similar for all tides.

Fig. 3.10 shows five time instances from dam closing experiments; the top panels show the case with no dam (ex. Gate0) and the bottom panels show the case with a dam that closes during early ebb (ex. Gate4b). The grayscale colormap shows surface source water concentration. In both experiments, source water is tagged until 1.55 hrs after high water, ensuring that all of the water that reaches the front over ebb is tagged (Fig. 3.8). At 1.55 hrs after high water, the gate is closed in the dam experiment and no additional water is released from the estuary mouth, but in the no-dam experiment the estuary-ocean exchange is maintained throughout ebb. The blue and red lines in both series of panels mark the position of the plume front in the dam and no-dam case; the front is defined by the contour where surface dye concentration is less than 10^{-5} in the no-dam case (ex. Gate0, dye tagging source water throughout ebb) and in the dam case (ex. Gate4b, dye tagging source water until HW + 1.55 hrs). In the no-dam case the source water overtakes the front, as seen in previous experiments, but in the dam case, comparatively little source water arrives at the front. Although the source water distribution is altered in the dam case, the front position (in the offshore direction) does not change greatly between the dam and no-dam case.

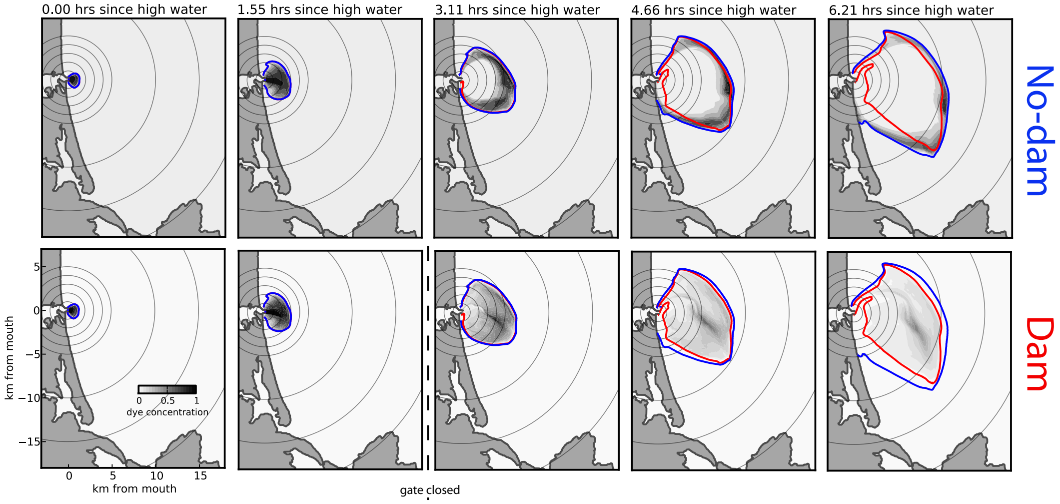

Figure 3.10: Top panels show a time sequence of surface dye concentration during experiment Gate4a and the bottom panels show surface dye concentration during experiment Gate4b, which is the same as experiment Gate4a but with a gate closed at the estuary mouth at 1.55 hrs after high water. Source water is tagged with dye until the time the gate is closed (in both experiments, although no gate is closed in the Gate4a experiment). The blue lines are the locations of the tidal plume front in the experiment without a gate and the red lines are the locations of the front in the experiment with a gate.

The additional results of three experiments, each closing the gate an hour apart during early ebb, are shown in Fig. 3.11. In the top panel, the green line shows the position of the front at the end of ebb (6.21 hrs after HW) for the case with a gate closing at 0.78 hrs after high water (ex. Gate1b), the red line shows the front in the gate closing at 1.81 hrs after high water case (ex. Gate2b) and the cyan line shows the gate closing at 2.85 hrs after high water case (ex. Gate3b). The blue line shows the front in the no-dam case. The dam affects the lateral expansion of the plume more than the offshore expansion and tidal plume frontal propagation.

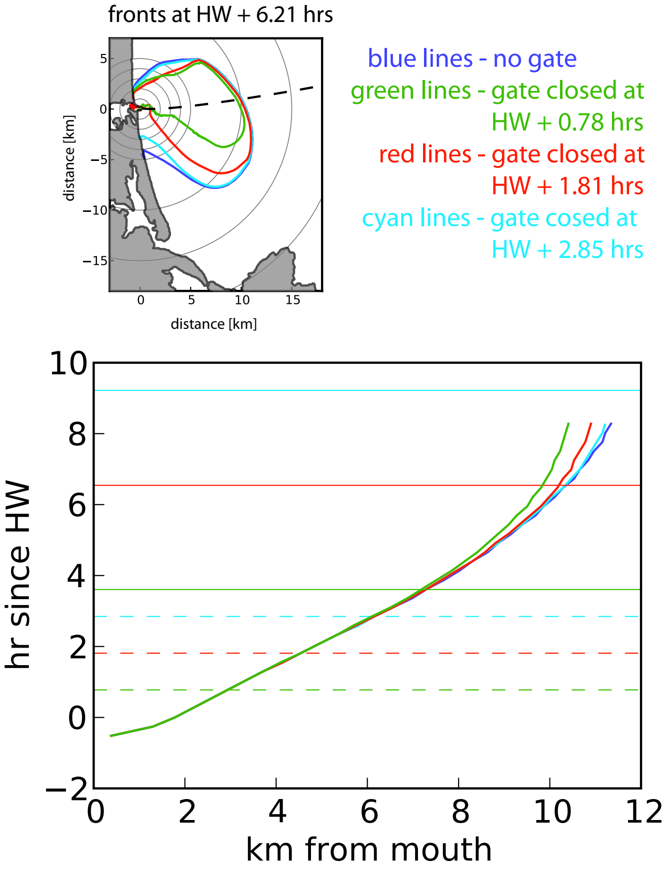

Figure 3.11: Top panel shows the position of fronts at 6.21 hrs after high water for four different gate experiments. Bottom panel shows a time series of the position of the fronts along an offshore transect (dashed line in top panel). The dotted lines in the bottom panel mark the times the gates are closed and the solid horizontal lines show the times when the source water blocked by the dam would have reached the front, given by the age relation in Fig. 3.8.

The front position along the offshore transect shown in the top panel (black, dashed line) is displayed as a function of time in the bottom panel of Fig. 3.11. The colored, dashed lines show when the gate is closed in each case and the solid lines show when water released at the gate closing time would have reached the front according to the age relation in Fig. 3.8 (the late gate closing at 2.85 hrs after HW is out of the release-arrival time range presented in Fig. 3.8 so it is extrapolated). The separation of the fronts occurs approximately when the source water blocked by the dam would have arrived at the front, indicating that when the gate is closed, the inertia of the source water already released is enough to supply the front and sustain its propagation.

3.4 Discussion

The numerical simulations in this study address the communication between the estuary mouth and the tidal plume front; the translation of source water through the plume is examined and the amount of source water that reaches the front over a single ebb is quantified. We also investigate the role of time dependent estuarine discharge on frontal propagation.

An important result of this study is the age relation presented in Fig. 3.8. The volume of water expelled from the estuary increases over ebb in relation to the tidal transport, but water released later than ∼2.5 hours after the start of ebb does not interact with the propagating front kinematically. However, the similar trend between mean plume speed and estuarine discharge illustrated in the bottom panel of Fig. 3.8, the slight increase in source water flux behind the front at max ebb illustrated in Fig. 3.9, and the different surface source water concentration between the dam and no-dam cases shown in Fig. 3.10 suggest that water released after this time does accelerate old source water frontward, possibly through the large pressure gradient emanating into the plume from the estuarine channel during max ebb. Although source water exhibits variable speeds across the plume, the mean translation speed of source water through the plume core is proportional to the timing and magnitude of estuarine discharge; a similar result is shown in Kilcher and Nash (2010) but the physical mechanism is still unclear. Water released after ∼2.5 hours after the start of ebb likely influences the evolution of the next tidal pulse as much as the current because it affects mixing as the ambient stratification receiving the next tidal pulse.

Fig. 3.9 shows that less source water is supplied to the front as ebb progresses because of source water spreading over an expanding plume body and increased dilution in the plume interior over this larger surface area. ∼6.5 % of discharge interacts with the front in the first six hours of ebb. Although this estimate is likely influenced by wind and discharge, and varies for each ebb, the small percentage suggests that the strong mixing Pritchard and Huntley (2006) and Orton and Jay (2005) measure at the plume front is only representative of frontal dynamics during a small portion of early ebb in the Merrimack. Since primarily ambient water is measured at the front in these numerical simulations, the late ebb mixing measured in previous studies must be between well diluted source water and ambient water converging at the front; this is a reasonable explanation if there is old, relatively-fresh plume water near the mouth, making the ambient ocean be a source of buoyancy as well as the estuarine discharge. These experiments indicate that, at least in terms of net mixing of the estuarine discharge through the tidal plume, the frontal mixing matters less than previously thought, and shear mixing in the near-field dominates. Supporting this idea, several ebbs shown in Fig. 3.3 demonstrate that the water overtaking the front is the same salinity of the front or saltier.

The gate experiments illustrated in Figs. 3.10 and Fig. 3.11 investigate the response of the front to changes in estuarine discharge directly. Fig. 3.10 shows that the difference in the offshore position of the fronts after ∼6 hrs of ebb are similar even, when the discharge is dammed early in ebb. Moreover, the front continues to propagate offshore, ignorant of the dam, for several hours before it relaxes. Fig. 3.11 indicates that the front begins to slow when it experiences the absence of the estuarine discharge blocked by the dam, as predicted by the age relation presented in Fig. 3.8. There is no immediate response in frontal propagation when the dam is closed; thus the estuarine discharge does govern frontal propagation, but with a lag, differing from the Kilcher and Nash (2010) hypothesis.

It is unclear why the front is not responsive to the dam immediately after it is closed; it appears that more source water approaches the front in the no-dam case in Fig. 3.10, and the estuarine discharge late in ebb clearly aids in propelling source water released during early ebb frontward according to the results illustrated in the bottom panel of Fig. 3.8. Perhaps the water overtaking the front is already mixed in the plume body such that it doesn't affect frontal propagation strongly without adding buoyancy. Further experiments to test this theory are necessary, but these results suggest that plume growth via the propagating front can be modeled quite simply, without linking the complicated dynamics of the source and near-field regions to it. A lagrangian frontal model such as the model presented in Jay et al. (2010) may be sufficient to estimate front behavior.

3.5 Conclusion

There are two primary findings of this study. First, more ambient water interacts with the tidal plume front than source water. Because it takes several hours for source water to translate the plume and it is strongly diluted in the plume body, only a small fraction of source water reaches the front. Second, the mouth and the front communicate on an advective time scale. When the estuarine discharge is arrested during early ebb in idealized dam experiments, the inertia of the discharge is enough to keep previously released source water necessary to sustain frontal propagation moving frontward.

Besides advancing understanding of gravity current behavior and fundamental knowledge of the spatial extent of a plume, as it is governed by the propagating front, these results have significant implications for the net mixing of estuarine discharge in the plume - when, where, how and how much mixing occurs. Variability in plume mixing over an ebb cycle is not well understood; previous studies of frontal mixing, structure and overtaking velocities in lee of the front (as well as most other aspects of tidal plume dynamics) typically focus on the max ebb phase of the tide and likely overestimate the significance of the front to net mixing of the total ebb discharge. This study clearly shows that the mixing and translation of source water though the plume body changes significantly over ebb, indicating that the dynamics of the front likely do as well with the source water supplied to it. It is reasonable to conclude that early in ebb the front contributes greatly to net mixing of the estuarine discharge, while later in ebb, as the maximum discharge is released, near-field net mixing is greater than frontal mixing.

This study supports the theory that kinematic communication between the estuary mouth and the tidal plume front persists throughout ebb, in agreement with observations. However, numerical simulations indicate that there is a lag in the frontal response to changes in the estuarine discharge because of the expanding plume body separating the two regions, as well as a greatly diminished quantity of ebb discharge overtaking the front due to shear mixing over the extensive plume base. Furthermore, the front propagation response to damming the source water at the mouth is surprisingly small, indicating that the initial formation of the front is key in determining its propagation offshore.

In addition to kinematic communication, information can travel between the estuary mouth and plume front dynamically through waves. It is not clear from observations if this type of communication exists in the Merrimack, but it is not addressed in this study because of model limitations.

4. THE EFFECT OF ROTATION ON NET PLUME MIXING

4.1 Introduction

Strong mixing in the region just seaward of a narrow estuarine discharge can significantly alter the water properties of a parcel, such that the water that eventually enters a geostrophic along-shore coastal current is substantially different from the water that left the estuary mouth. Much of this mixing happens in the near-field river plume, a region of rapid plume expansion and strong shear mixing. The asymptotic limit of these properties signals the transition to the far-field where the riverine water becomes part of the larger scale shelf circulation. There are many different ways to estimate the scale of the near-field plume; for example, the transition from super to subcritical flow in the plume commonly signals the end of the near-field. Generally, the residence time of fresh water in the near-field plume is on the order of hours, which may be short relative to the time spent in the estuary and other coastal regions, yet the change in salinity of a water parcel as it traverses the near-field is dramatic because of intense shear mixing. This paper focuses on how estuarine discharge is transformed as it passes through the near-field, which in part defines the water properties of the subsequent coastal current. Many models of coastal buoyancy-driven flow use source parameters, such as the density anomaly and discharge rate, to predict the properties of shelf circulation (e.g., Garvine, 1987; Yankovsky and Chapman, 1997; Lentz and Helfrich, 2002). Mixing in the near-field plume may substantially alter the estuarine discharge properties, and thus, influence subsequent buoyancy-driven shelf circulation.

The 'net' mixing that a water parcel experiences as it transitions through the near-field plume is proportional to, but distinct from the 'local' mixing at a single point, as the net mixing depends on the mixing history of a water parcel and the length of time that particle stays within the near-field plume. The net mixing may be defined as the change in plume density anomaly between the estuary mouth and the point where strong mixing has diminished; where a water parcel enters the coastal current or far-field plume. The transition region between the near- and far-field is the mid-field; it is composed of both near- and far-field dynamics. Although the strongest mixing occurs in the near-field close to the source, since mixing slows in the mid-field, the dilution through this region also impacts net mixing of a plume water parcel.

The temporal evolution of plume spatial structure is affected by atmospheric forcing, rotation, ambient flow and tidal currents outside the mouth (O'Donnell, 1990; Fong and Geyer, 2001; Garcia Berdeal et al., 2002; Choi and Wilkin, 2007; Zhang et al., 2009); these physical elements force the mid-field and can alter plume expansion through advection and effectively arrest shear mixing. Estuarine mixing sets the density structure at the river mouth and therefore influences near-field processes and plume propagation from its early formation. Furthermore, remnants of far-field plumes from previous tidal cycles modify the stratification on the inner shelf encountered by a tidal plume, and therefore influence the near-field shear stratified mixing environment (Horner-Devine et al., 2009).

Classic modeling studies of buoyant plumes examine the affect of varying inflow properties on plume evolution offshore (Garvine, 1982, 1987; O'Donnell, 1990; Yankovsky and Chapman, 1997; Jirka, 2007; Jones et al., 2007), but none focus specifically on net mixing trends. These studies describe the response of a plume to changes in transport, buoyancy and momentum fluxes at the mouth in Cartesian space, with descriptions of lateral and vertical structure and measures such as jet-to-plume length scale and plume cross-shore spatial scale. Plume parameters integrated over isohalines were first used by Hetland (2005) to study the plume response to wind; inflow variability was not examined. Yankovsky et al. (2001) investigate the impact of tidal and subinertial variations in discharge on plume structure using both pulsed harmonic forcing and single pulsed discharge events. Although plume mixing is not considered directly, they conclude that subinertial variability in estuarine discharge greatly affects bulge dynamics and downstream circulation through the generation of the density field.

Local mixing estimates in near-field plumes are well established in literature (Chen and MacDonald, 2006; MacDonald et al., 2007; McCabe et al., 2008), but recent observational (Halverson and Pawlowicz, 2008) and modeling (Hetland, 2010) studies show disagreement between net mixing trends. Halverson and Pawlowicz (2008) show that the Fraser River plume density anomaly increases with discharge in the Strait of Georgia, BC, Canada from several years of ferry data. Hetland (2010) reports the opposite trend in net plume mixing using an idealized near-field layer model. There are several differences in experimental approach between the two studies; one being that rotation is not incorporated into the layer model formulation, while the field measurements describe observations of a geophysical scale plume, obviously influenced by rotation. Although observational and modeling studies show that rotation is an important factor in the plume momentum balance even within a kilometer of the estuary mouth (Chen et al., 2009; McCabe et al., 2009), it is often overlooked in studies of near-field mixing driven by advection and buoyancy. Though it may not strongly impact local mixing rates close to the source, rotation may affect spreading by turning the plume to the coast, curtailing the enhanced mixing that spreading causes, and thereby impacting net plume mixing estimates greatly.

In this paper, the role of rotation in arresting near-field mixing is examined as the most likely cause for the disagreement between the two studies by Halverson and Pawlowicz (2008) and Hetland (2010). Both Halverson and Pawlowicz (2008) and Hetland (2010) show that the near-field region grows proportionally to river discharge, suggesting an increased transit time of flow in the near-field. However, geostrophic adjustment occurs at timescales of f^{-1} – independent of discharge – turning the flow anticyclonically, and arresting plume spreading by trapping the plume to the coast. Rotation will therefore limit the area over which plume spreading and enhanced shear mixing takes place. We use numerical simulations to quantify net plume mixing in rotational and irrotational experiments while varying fresh water discharge. Ambient flow and tides are other important elements that influence the Fraser plume structure and evolution that we incorporate into our experiments, but Halverson and Pawlowicz (2008) assert that the wind driven circulation in the enclosed strait is likely different than the shelf plume response, therefore the affect of the wind directing and mixing plume waters is not considered in this study.

4.2 Numerical setup

The numerical simulations use the Regional Ocean Modeling System (ROMS, version 3.5) (Shchepetkin and McWilliams, 2005), configured with a rectangular grid that represents an estuary/shelf plume system. ROMS is a hydrostatic, free surface, primitive equation model that is commonly used in coastal studies of buoyancy driven flow. The domain is idealized, but supports plume dynamics similar to the Merrimack (Hetland and MacDonald, 2008) and Columbia River (McCabe et al., 2009) discharges. The dimensions of the domain are based on the Merrimack River estuary and plume, with a narrow estuary mouth opening separating a wider estuary from the shelf. Fig. 4.1 shows the model domain.

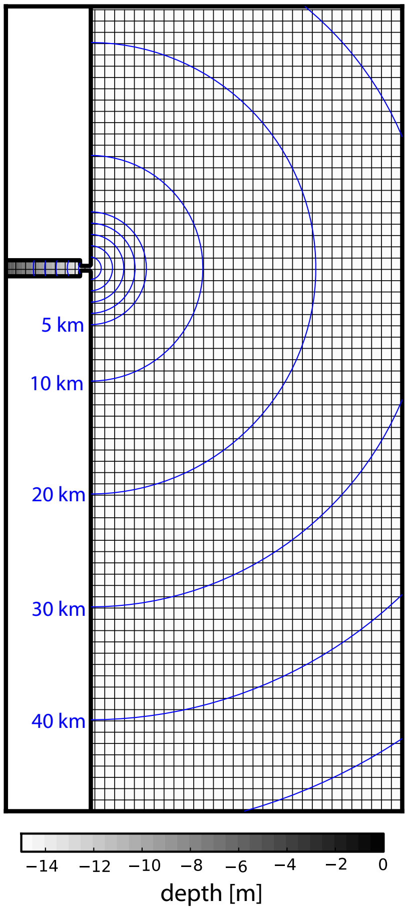

Figure 4.1: Model grid and bathymetry. Black lines mark every 10 grid spaces. Blue lines are radial distances from the mouth in kilometers (1, 2, 3, 4, 5, 10, 20, 30, 40, 50 km shown). Gray filled contours indicate water depth.

The grid is 35 km long in the cross-shore direction and 71.2 km long in the alongshore direction with a horizontal grid spacing of 100 m in both directions, and open boundaries upcoast, downcoast and offshore. The river discharge is specified at the western edge, at the upstream end of the estuary. The simulations use 20 irregularly spaced vertical layers stretched at the free surface and the bottom, with $\theta_s = 3.0$, $\theta_b = 0.25$, and $h_c = 5$ m. Bottom topography is flat at 15 m depth over the shelf and linear in the estuary with a minimum 5 m depth at the head and maximum 15 m depth at the mouth. The estuary is rectangular with a contraction at the mouth

500 m wide and 1 km long; the total length of the estuary is 8.5 km. Rotating experiments are performed on an f-plane with $f = 10^{-4}$ s^{-1}.

The plume develops through riverine buoyancy forcing, with ambient salinity of 32 g kg^{-1} initialized in the oceanic portion of the domain and fresh water of 0 g kg^{-1} entering the domain at the head of the estuary. Modeled salinities are reported on the Absolute Salinity scale. A semidiurnal tide is incorporated into the model by raising and lowering the free surface at the open boundaries as a sine wave with a 12 hr period; the tidal phase is referenced to the sea surface height at the estuary mouth in the following analyses. A 5 cm s^{-1} southward flowing barotropic coastal current that spans the oceanic portion of the domain is forced at the northern open boundary. Flather and Chapman conditions are applied at the open boundaries for the barotropic velocity components and free surface, respectively, which allows fluid flow out of the domain (Flather, 1976; Chapman, 1985). Three dimensional velocity components and tracers follow a radiation open boundary condition (Marchesiello et al., 2001). The model is initialized to oceanic salinity, a flat sea surface and a 5 cm s^{-1} downcoast flow.

Vertical mixing is described by $k - \epsilon$ turbulence closure coupled with Canuto-A stability function formulation (Canuto et al., 2001). Quadratic bottom friction is incorporated into the momentum equation and conservative, parabolic spline reconstruction is used for vertical derivatives in the model. A small background horizontal laplacian diffusion of tracers with a coefficient of 1 m^2 s^{-1} is used to damp numerical instabilities, with horizontal mixing of tracers along geopotential surfaces. Horizontal and vertical tracer advection are calculated using MPDATA (Smolarkiewicz and Clark, 1986).

Each simulation is run for approximately one week. For most of the analyses, model simulations are evaluated over two averaged tidal cycles on the fifth day of the simulation. Several experiments vary the river discharge into the estuary. Discharge rates of Q_f = 100, 250, 500, 1000, 1800 and 2800 $\mathrm{m}^3\ \mathrm{s}^{-1}$ are implemented in the model paired with a 1.5 m tide. Fig. 4.2 illustrates low and high discharge scenarios over a tidal cycle. Table 4.1 shows tidal mean inflow parameters for the experiments. $R_d = \sqrt{g'h}/f$ is the baroclinic Rossby radius of the inflow, where f is the rotational frequency, $g' = g\Delta\rho/\rho_0$ and h are reduced gravity and depth at the estuary mouth, g is gravity, $\Delta\rho$ is the inflow density anomaly and ρ_0 is the ambient density. $R_o = U/fW$ is the mouth Rossby number, where U is the mean velocity of the inflow and W is the mouth width. $S = R_d/W$ is the Burger number of the inflow and $Fr = R_o/S = U/\sqrt{g'h}$ is the inflow Froude number. The large values for R_o and S indicate that rotation has little effect near the source; the small mouth width significantly constricts the flow, creating a strong jet-like discharge. However, the buoyancy of the inflow influences plume evolution more than advection, given the subcritical inflow Froude numbers; this is evidenced by the surface advected plumes shown in Fig. 4.2 (Yankovsky and Chapman, 1997).

The zero salinity contour occurs inside the estuary in the low-medium discharge cases, as well as the plume lift off. Plume dynamics are altered in the different discharge cases by the amount of ocean water able to enter the estuary and be subsequently mixed into the upper layer that feeds the plume. Mixing dynamics are also affected in the plume by bottom advection offshore in high discharge cases, but we assume that near-field interfacial mixing is the dominant mixing process that salinates plume waters; it is the biggest contributing process to net mixing in all cases. The purpose of the model is to investigate bulk plume properties by integrating over the entirety of the plume through a large parameter space; a goal not easily accomplished with observations. Net mixing is defined as a measure of the change in plume density strictly between the estuary mouth and coastal current;

Table 4.1: Tidal mean dimensional and nondimensional parameters at the inflow for rotational experiments. Columns show river discharge, the baroclinic deformation radius (R_d), the Rossby number (R_o), the Burger number (S) and the Froude number (Fr).

Discharge (m^3 s^{-1})	R_d (km)	R_o	S	Fr
100	11.08	7.66	22.17	0.35
250	14.57	10.79	29.15	0.37
500	17.10	14.30	34.20	0.42
1000	18.81	18.67	37.63	0.50
1800	19.08	22.99	38.15	0.60
2800	19.09	26.59	38.18	0.70

water properties at the inflow are the forcings considered in parameter space. It is expected that the dynamics of each plume experiment varies slightly due to the location of the zero salinity contour and lift off; much of the variability is brought on by the geometry (and bathymetry) of the estuary, which is designed, in this case, to reflect an idealized Merrimack River estuary.

Experiments with and without rotation are performed. Fig. 4.3 shows an example of surface salinity from two experiments with the same discharge ($Q_f = 1000$ m^3 s^{-1}); with and without rotation. The extent of the spreading plume region is significantly different between the two cases. In the $Q_f = 1000$ m^3 s^{-1} case, the distance from the mouth to the 32 g kg^{-1} contour in the offshore direction is ~16 km in the rotational case, while the 32 g kg^{-1} contour leaves the domain in the irrotational case. The plume covers approximately twice as much area between the rotational and irrotational cases for the $Q_f = 100$ m^3 s^{-1} discharge case (not shown), and the difference in surface area grows with discharge. In the $Q_f = 1000$ m^3 s^{-1} case (Fig. 4.3), the tidal mean plume area within the 32 g kg^{-1} contour covers ~41% of the ocean domain in the rotational case and ~90% in the irrotational case, though the contours interact with the boundary in the irrotational case at peak ebb.

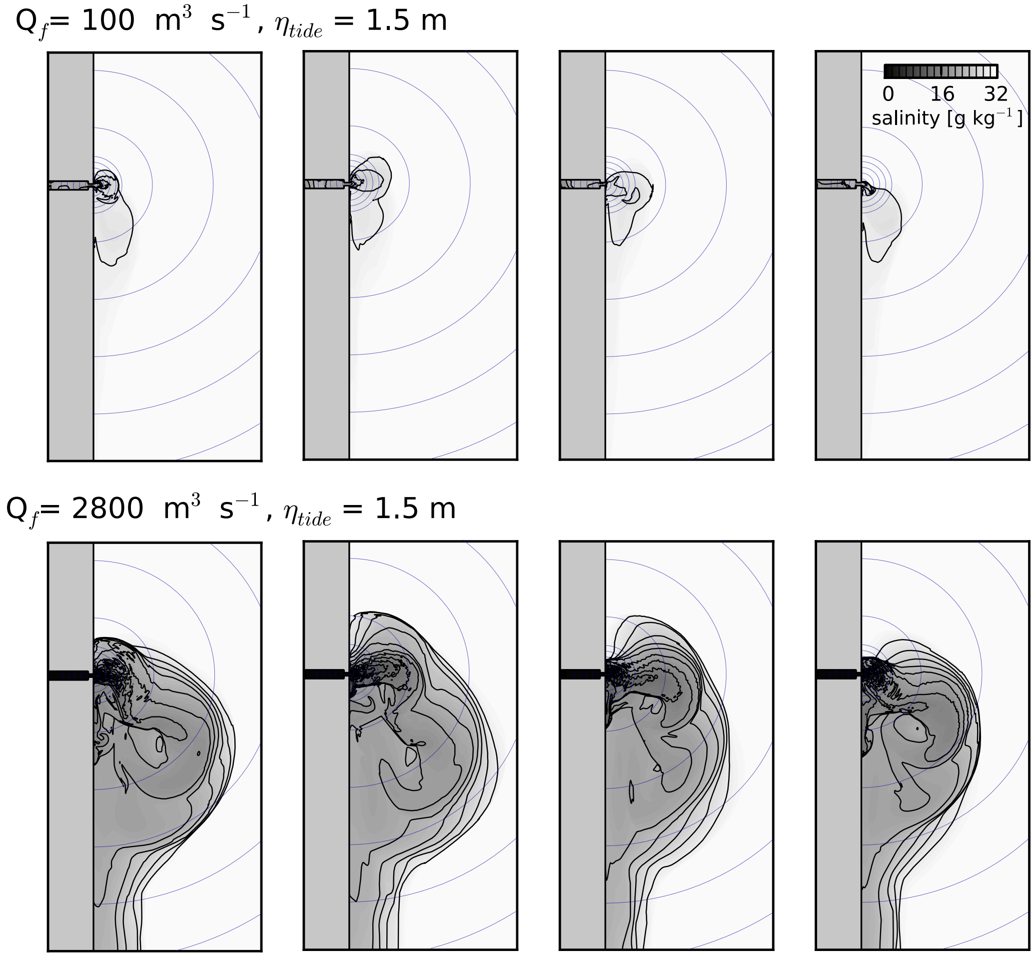

ebb *slack* *flood* *slack*

Figure 4.2: Time sequence of surface salinity for the $Q_f = 100$ m^3 s^{-1} (upper panels) and $Q_f = 2800$ m^3 s^{-1} (lower panels) rotational cases. Far left panels show surface salinity at max ebb, center left panels show surface salinity at low water, center right panels show surface salinity at max flood and far right panels show surface salinity at high water. Phases of the tide are labeled with respect to the sea surface elevation at the center grid cell at the estuary mouth. Blue lines are radial distances from the mouth (same shown as Fig. 4.1).

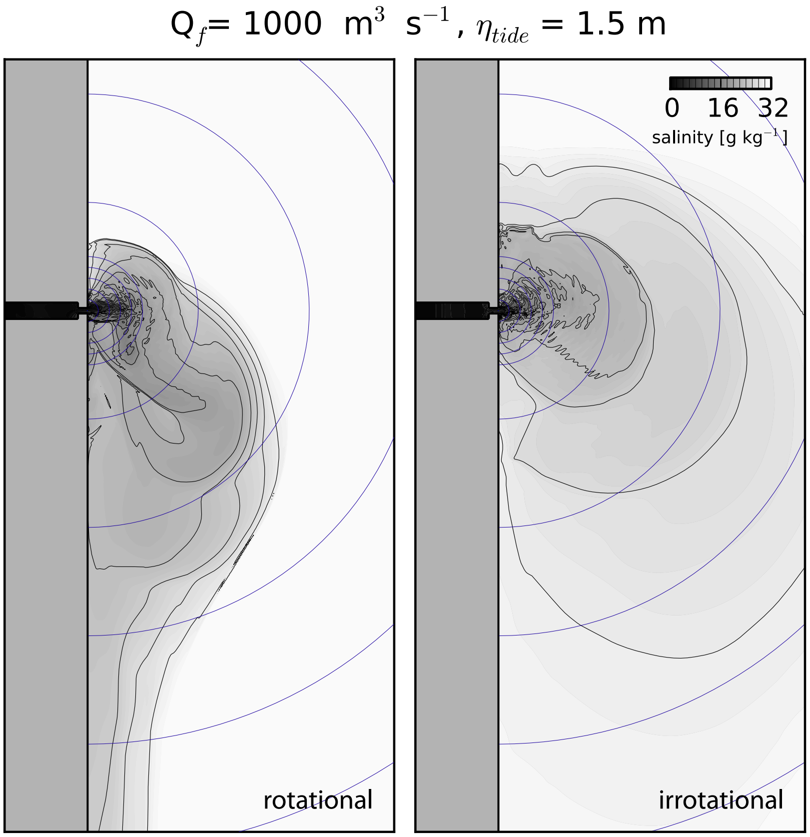

Figure 4.3: Surface salinity at late ebb for Q_f = 1000 m^3 s^{-1} experiments with and without rotation. A 5 cm s^{-1} southward flowing barotropic coastal current is forced at the northern boundary. Blue lines are radial distances from the mouth (same shown as Fig. 4.1).

4.3 Results

4.3.1 Plume isohaline structure

In this section we examine the distribution of fresh water in salinity space as it is mixed with background waters in rotational experiments. Estimation of net plume mixing requires a robust definition of the near- and mid-field plume, and a salinity-based coordinate system is well-suited to define dynamic plume regions because it expands and moves with the various dynamic regions (Hetland, 2005). Fresh water volume is tracked through salinity space to identify salinity classes where fresh water pools (e.g., the bulge region) and where it is quickly flushed to higher salinity classes through vigorous mixing with background waters (e.g., the intense mixing region near the estuary mouth). Thus, dynamic plume regions may be inferred from the distribution of fresh water in salinity coordinates.

When brackish water exits the estuary, the plume expands as a gravity current, as it is no longer confined by the estuarine channel (Hetland and MacDonald, 2008). The spreading plume causes the pycnocline to shoal, and the sea surface to drop. This drop in pressure, a decrease in the potential energy of the plume, causes a corresponding acceleration of the plume due to an increase in the kinetic energy, as described by the Bernoulli relation. The accelerating plume increases the shear at the base of the plume, thereby enhancing shear instabilities and mixing within the plume. This relationship between plume spreading and mixing is discussed in detail by Hetland (2010). Generally, the strength of mixing decreases offshore and the separation between isohaline outcroppings increases. Eventually, in the absence of other forces, as the near-field plume returns to subcritical flow and local mixing rates decrease, the density anomaly associated with the near-field plume asymptotically approaches its far-field value. However, as we show below, rotation may arrest the plume spreading, and consequently shear mixing, prior to its reaching the non-rotational far-field asymptotic limit.

The cartoon in Fig. 1.1 illustrates a vertical section through the core of the plume during ebb, with an axially varying, slab-like plume salinity structure and a thin pycnocline, similar to that discussed by Hetland (2005). In a steady state, the vertical mixing within the plume may be related to the surface area of different salinity classes within the plume; a relationship given by

$$w_e(s_0 - s_A)\frac{\partial A}{\partial s_A} \sim Q_f, \tag{4.1}$$

where $w_e(s_0 - s_A)$ is the average vertical salt flux associated with the surface salinity range s_A, s_0 is the background salinity, w_e is the vertical entrainment velocity, A is the surface area of salinity range s_A and Q_f is the river discharge. Thus, the regions of rapid change in surface salinity are associated with high mixing. Because the plume thickness remains relatively constant compared to changes in its horizontal extent, a similar relationship holds for the volume of different salinity classes. A large volume of water at a particular salinity indicates waters associated with weak mixing.

The left and bottom right panels of Fig. 4.4 show surface salinity and a vertical section of salinity in the $Q_f = 500$ m^3 s^{-1} idealized plume simulation during mid ebb. The vertical salinity structure in the plume along the transect, marked by the dotted line in the left panel, is similar to the vertical structure illustrated in the cartoon in Fig. 1.1, and the resultant isohaline fresh water volume distribution is similarly decomposed into plume regions. The transition between dynamic plume regions is chosen from an evaluation of isohaline differential fresh water volume. The upper right panel of Fig. 4.4 shows differential fresh water volume on a log scale. Salinity is divided into 1 g kg^{-1} bins. Each black line represents a different hour during a tidal cycle (12 lines shown) and the bold black line is the tidal mean. The red line corresponds to a time during mid ebb. Isohaline differential fresh water volume is essentially a histogram of fresh water volume as a function of salinity (MacCready et al., 2002; Hetland, 2005). The differential fresh water volume, $\partial V_f / \partial s_A$, is evaluated from a volume integration of the fresh water fraction,

$$V_f(s_A) = \int_{s \leq s_A} \frac{s_0 - s}{s_0} dV. \tag{4.2}$$

An analogy can be made where the total fresh water contained within an isohaline,

V_f, is similar to a cumulative probability distribution, and the differential fresh water volume, $\partial V_f/\partial s_A$, is then like a probability distribution function. Simply explained, V_f gives the cumulative fresh water volume in an isohaline spanning many salinities down to the fresh endmember, while $\partial V_f/\partial s_A$ gives the fresh water content in the smaller range ∂s_A; $\partial V_f/\partial s_A$ is a 'differential' fresh water volume, as termed in previous studies using isohaline coordinates (MacCready et al., 2002). The differential fresh water volume distribution can be interpreted as a histogram of fresh water content over the range of isohalines in the model domain. The surface of the isohaline, s_A, is the bound for integration, and $s_0 = 32$ g kg^{-1} is the oceanic reference salinity. The transparent lines show fresh water volume for isohalines throughout the model domain (estuary and plume) and the bold lines show the calculation for the oceanic region of the domain (plume only). Note that the largest differential fresh water volume occurs at s_0, but this peak is removed to focus on plume isohalines.

The 'plume only' fresh water volume distribution is consistent with the thin, surface trapped plume structure depicted in Fig. 1.1. The small fresh water volume in isohalines between 0 and 16 g kg^{-1} corresponds to the very near-field of the plume. Here water is quickly mixed and flushed to higher salinity classes. Fresh water is stored in offshore isohalines greater than ∼16 g kg^{-1}. The slope of the fresh water volume distribution up to ∼27 g kg^{-1} is a reflection of the expansion of plume isohalines offshore as mixing slows, consistent with the exponential decay of plume density anomaly away from the source shown in previous studies (Hetland, 2010). The peak in fresh water volume around 27 g kg^{-1} indicates the point in the plume where mixing is reduced and fresh water pools; the color bar in the top right panel is split from blue to gray at this salinity. Visual examination of surface salinity shows that the the peak occurs at the salinity of water entering the coastal current, conveying that water fresher than 27 g kg^{-1}, for the $Q_f = 500$ m^3 s^{-1} case, comprises the near- to mid-field plume. The mixing from the salinity at the estuary mouth to 27 g kg^{-1} is used as an estimate of the net mixing in the plume. The diminishing entrainment offshore in this salinity range is further investigated later in this section. Fresher water near the source is rapidly mixed to a salinity of 27 g kg^{-1}, however, reduced local mixing at that salinity class requires a correspondingly larger surface area to mix fresh water to yet higher salinity classes. As seen in Fig. 4.4 (left panel), this salinity class represents the edge of the bulge region of the plume, and is characteristic of water entering the coastal current.

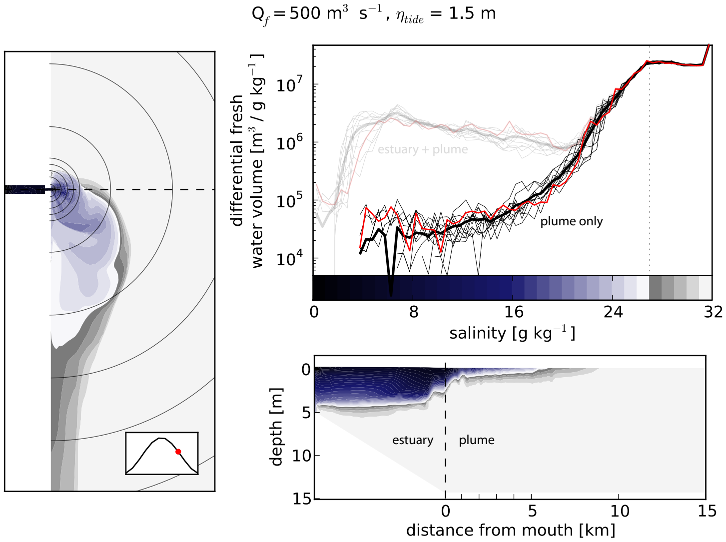

Figure 4.4: Panel on left shows surface salinity at mid ebb for the $Q_f = 500$ m^3 s^{-1} experiment with rotation (time is indicated by red dot on inset panel showing sea surface elevation over a tide). Bottom panel shows a cross section of salinity at mid ebb through the transect marked by the dotted line in the left panel. The top panel shows fresh water volumes in isohalines. Thin, black lines represent isohaline fresh water volumes hourly during a tide and the thick, black line shows the tidally averaged fresh water volumes. The red line marks fresh water volumes at mid ebb (same time as the other panels). The transparent cluster of lines illustrate domain-wide fresh water volumes in isohalines and the bold lines show fresh water volumes in isohalines in the oceanic portion of the domain. The split in the colorbar corresponds to the peak in fresh water volume that corresponds to the salinity of water entering the coastal current.

The salinity of water entering the coastal current is different for various Q_f experiments. Fig. 4.5 shows a composite of tidal mean differential fresh water volume from seven experiments varying Q_f. The curves are colored by fresh water flushing times, T_f, defined by

$$T_f = \frac{V_f}{Q_f}, \tag{4.3}$$

where V_f is an isohaline fresh water volume.

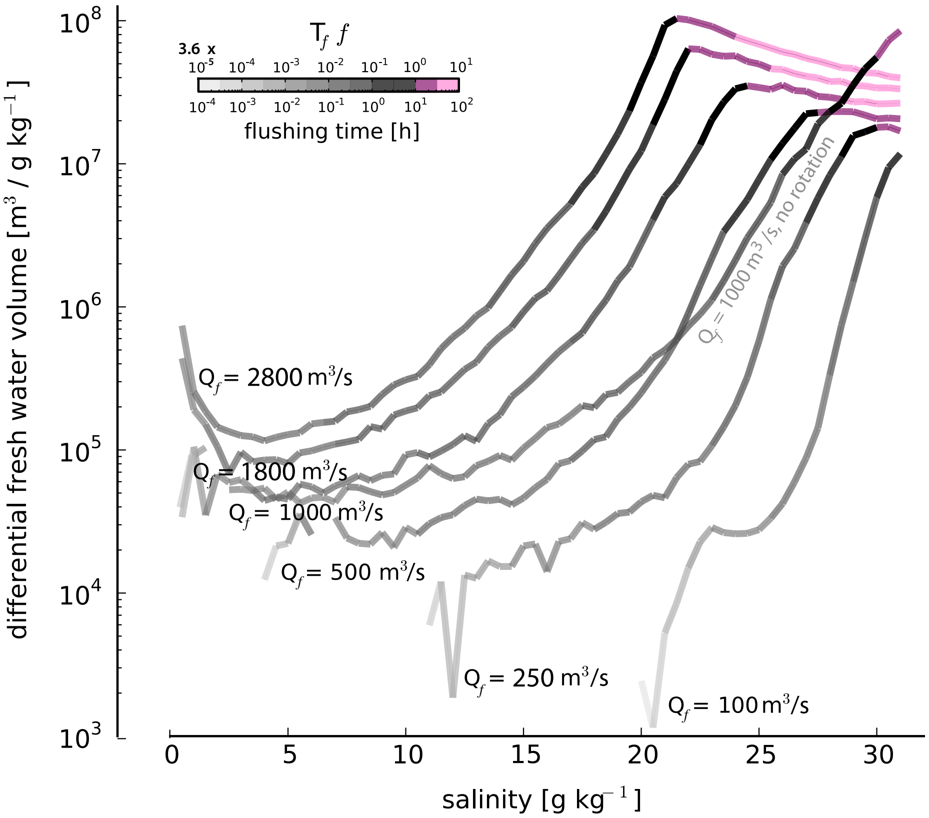

Figure 4.5: Tidal mean differential fresh water volumes for different discharge experiments with rotation. The $Q_f = 1000\ \mathrm{m^3\ s^{-1}}$ case is shown with and without rotation. Colors indicate flushing times of fresh water in isohalines (labeled on the bottom of the colorbar). The pink colormap indicates flushing times greater than the inertial period (far-field region). The top of the colorbar shows time scales normalized by the rotational parameter, $f \sim 10^{-4}\ \mathrm{s^{-1}}$.

The peak salinity of fresh water storage (the salinity of water entering the coastal current used to estimate net plume mixing) freshens as the discharge increases, indicating a fresher coastal current in each case. The nondimensionalized flushing time (T_f/f scale on top of the colorbar) indicates that the isohalines with peak fresh water storage flush fresh water on time scales close to the inertial period (∼17.5 hrs). Isohaline fresh water volume distributions in Fig. 4.4 show tidal variability is diminished relative to the mean at the peak, as compared to fresher salinities, further supporting the division between the near-/mid-field recirculation region and the far-field coastal current.

Following Eq. (4.1), the sea surface isohaline area is used to evaluate the entrainment rate at the plume base. The top panel of Fig. 4.6 shows the differential surface area of isohalines, $\partial A/\partial s_A$, in the ocean domain. The bottom panel of Fig. 4.6 illustrates decreasing entrainment as a function of surface salinity, as illustrated in Fig. 1.1, and is consistent with the plume regions defined by the flushing time scales in Fig. 4.5. Note that for the rotational $Q_f = 1000$ m^3 s^{-1} case, mixing decreases more rapidly as a function of salinity compared to the irrotational case with the same discharge (dashed lines in Fig. 4.6). The local entrainment velocities for this case are similar for salinity classes lower than 10 g kg^{-1}, but are nearly an order of magnitude different for salinities near 20 g kg^{-1}.

Net plume mixing is determined by a water parcel's local mixing rate, integrated over the area where mixing takes place. The net mixing is thus related to the total density (or salinity) change of the water between the estuary mouth and the coastal current where mixing is significantly suppressed. The scale of the supercritical plume region is compared directly between rotational and irrotational experiments in Fig. 4.7.

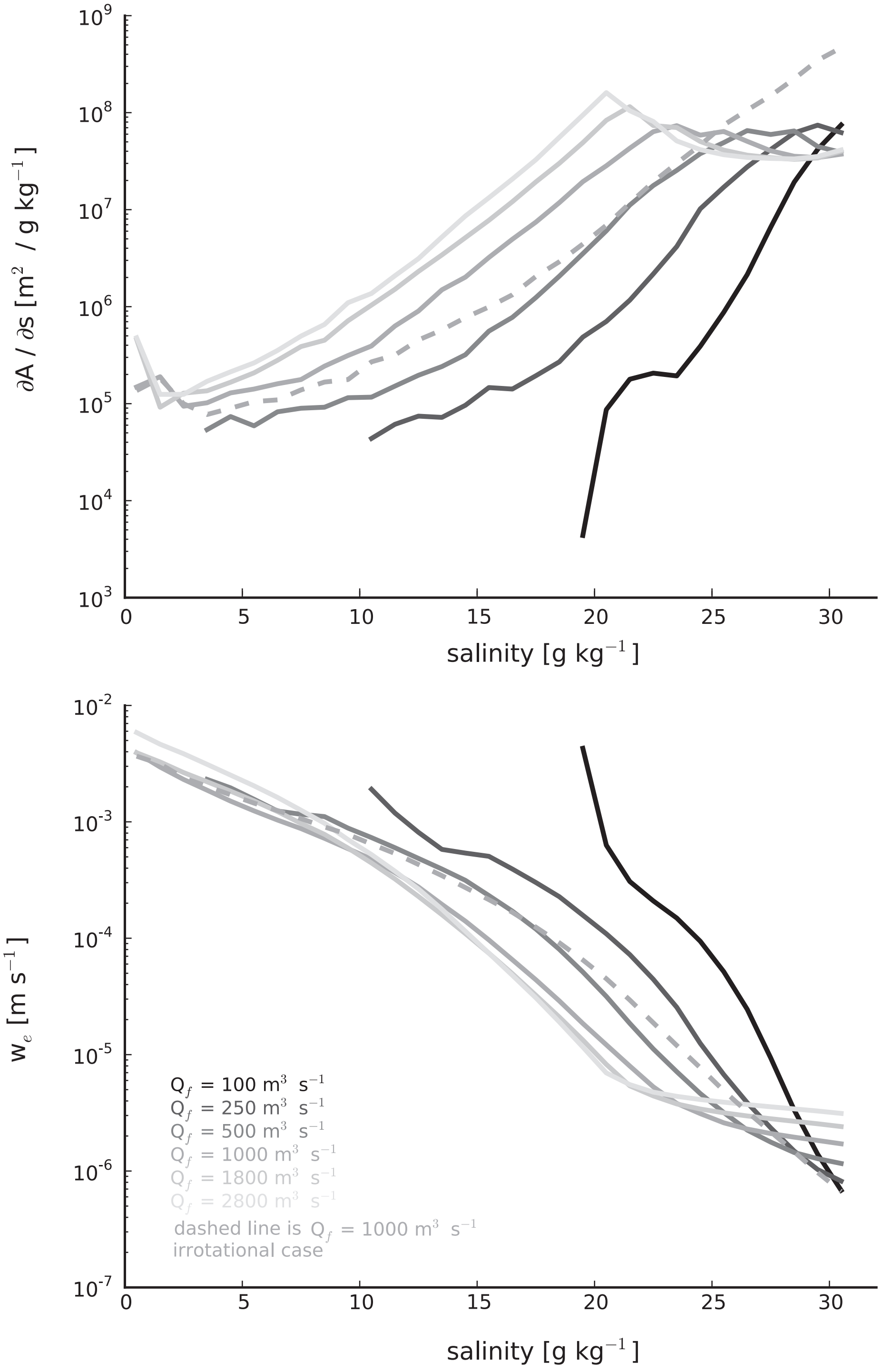

Figure 4.6: Tidal mean differential isohaline surface area (top panel) and mean entrainment velocity over the isohaline base (bottom panel) for rotational experiments with different discharges. Dotted line shows the $Q_f = 1000$ m^3 s^{-1} irrotational case.

The net mixing estimate gives the plume dilution integrated over the near-field region defined by a supercritical Froude number as

$$Fr = \frac{u}{\sqrt{g'h}} = 1, \tag{4.4}$$

where u is the plume layer vertically averaged velocity in the along-stream direction. Modeled velocities are rotated to the principle axis of variability calculated at the surface and then averaged in the plume layer. The plume layer depth, h, and reduced gravity, g', are calculated using the method described in Umlauf et al. (2007) and Hetland (2010). The first and second moments of the density anomaly, $\Delta\rho$, are evaluated using

$$\Delta\rho h = \int_{-H}^{\eta} (\rho_0 - \rho) dz \tag{4.5}$$

and

$$\frac{1}{2}\Delta\rho h^2 = \int_{-H}^{\eta} (\rho_0 - \rho) z dz, \tag{4.6}$$

where z is the vertical coordinate and integration is from the sea surface η to the ocean bottom H. The background density, ρ_0, is the density corresponding to the ocean reference salinity ($s_0 = 32$ g kg^{-1}).

Fig. 4.7 shows a scatter of the Froude number by surface salinity class averaged over ebb within a 90° angle offshore from the mouth for the $Q_f = 1000$ m^3 s^{-1} and $Q_f = 2800$ m^3 s^{-1} experiments with (blue) and without rotation (red). After rising to about 1.5, the Froude number generally gets smaller offshore. High Froude numbers at individual points offshore are a result of local fronts where the plume layer is eroded and should be disregarded; the Froude number at grid cells where $g' < 10^{-2}$ m s^2 are not shown. The location of the red-black and blue-black lines (highlighting an offshore transect from the mouth) crossing $Fr = 1$ roughly indicates the salinity where the transition from the near- to mid-field takes place (Hetland, 2010).

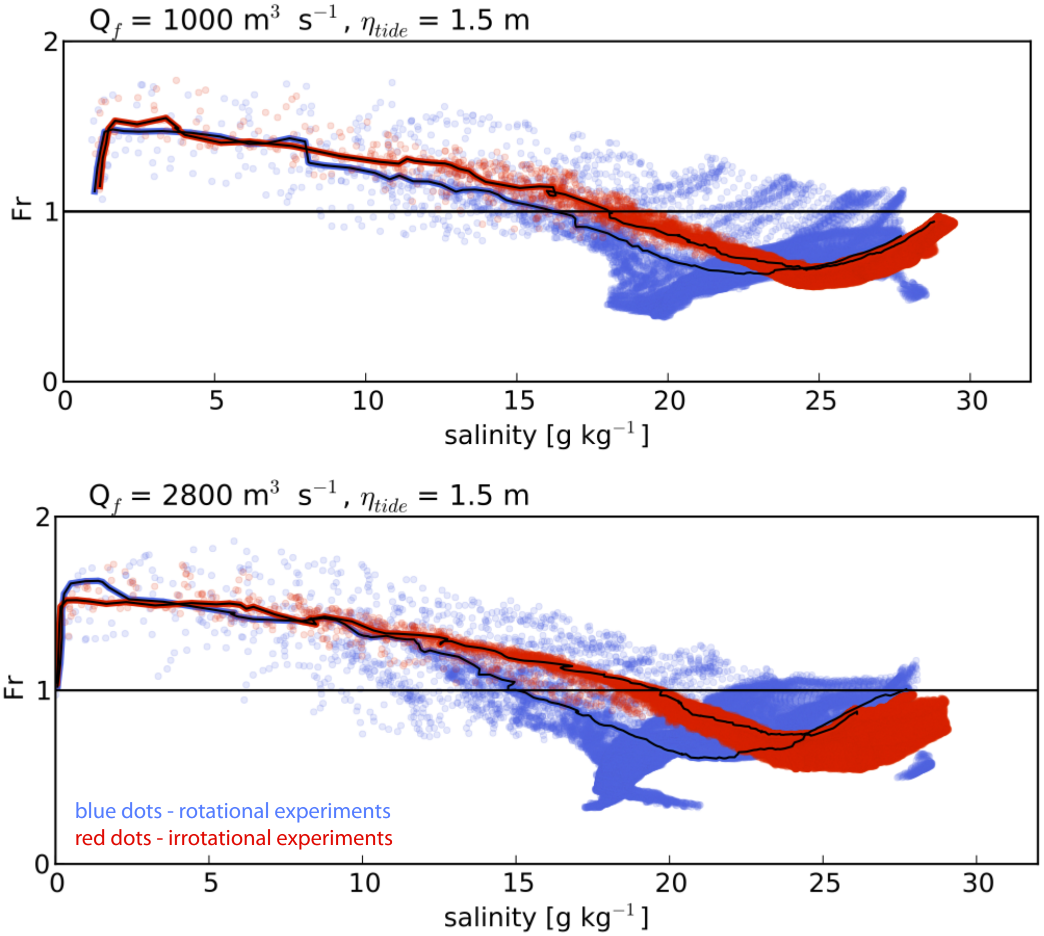

Figure 4.7: Mean (over ebb) upper layer Froude number for $Q_f = 1000$ m^3 s^{-1} and $Q_f = 2800$ m^3 s^{-1} experiments. Blue and red dots are domain wide upper layer Froude number for experiments with and without rotation respectively. Red-black and blue-black lines show the upper layer Froude number along a transect in the offshore direction from the mouth. Black horizontal line marks where $Fr = 1$.

For the low discharge experiments ($Q_f = 100$ m^3 s^{-1} and $Q_f = 250$ m^3 s^{-1}), rotation does not strongly affect the location of the transition from the near-field (not shown). However, as the discharge is increased, the location varies. The non-rotational experiments transition to subcritical at higher salinity classes, compared to the rotational cases with the same discharge. This spread in salinity class where the plume transitions back to subcritical between rotational and non-rotational cases grows as the discharge increases. The Q_f=2800 m^3 s^{-1} case has a span of approximately 5 g kg^{-1} at the point of return to critical flow between the rotational and non-rotational cases, the Q_f=1000 m^3 s^{-1} has a spread of approximately 1 g kg^{-1}. The Froude number defined near-field transition occurs at a lower salinity than the fresh water pools observed in Fig. 4.5, but it is not the actual transition salinity, but the trends between experiments that is the focus of this research. The definition of near-field used matters little when comparing tendencies in parameter space because they all scale similarly, thus the net mixing trends illustrated are robust.

Fig. 4.8 shows the vertical buoyancy flux for the $Q_f = 1000$ m^3 s^{-1} and $Q_f = 2800$ m^3 s^{-1} cases with and without rotation as a function of salinity class. Vertical turbulent buoyancy flux, B, is given by

$$B = -\frac{g}{\rho_0} K_\rho \frac{\partial \rho}{\partial z}, \tag{4.7}$$

where K_ρ is the eddy diffusion coefficient, or turbulent diffusivity of salt, since there is no temperature stratification. K_ρ is calculated from the turbulent kinetic energy, a turbulent length scale, and the stability function described in Section 3.2. B is calculated at each grid cell, binned by salinity, and the volume weighted mean value is calculated in each isohaline. The range of values of plume integrated vertical turbulent buoyancy flux is smaller than local shear mixing estimates in fronts and near-field plumes reported in MacDonald and Geyer (2004) and MacDonald et al. (2007), but reasonable for an isohaline average, since salinity classes also represent water outside of the vigorously mixed plume core. Isohalines of near-oceanic salinity interact with the boundary in irrotational cases, so mean isohaline vertical turbulent buoyancy flux should be interpreted with caution for salinities greater than 25 g kg^{-1} in the high discharge cases, marked as boundary interaction in Fig. 4.8.

Comparing cases with the same discharge indicates that the local mixing at high salinity classes is nearly an order of magnitude larger in the irrotational cases than in the rotational cases (around 20 g kg^{-1}). The near-field is identified as a region of strong shear mixing, and the drop in mixing at salinity classes near 20 g kg^{-1} in the rotational cases indicates the arrest of the near-field. Notice that the arrest occurs at a lower salinity in the high discharge case. In the irrotational experiments, the transition to the far-field happens gradually, but at a higher salinity in the high discharge case, evidenced by the shift to the right from the black to gray dotted line at high salinities. These trends are mirrored in the Froude number transition from critical to subcritical (Fig. 4.7) and experiments with different Q_f give similar results.

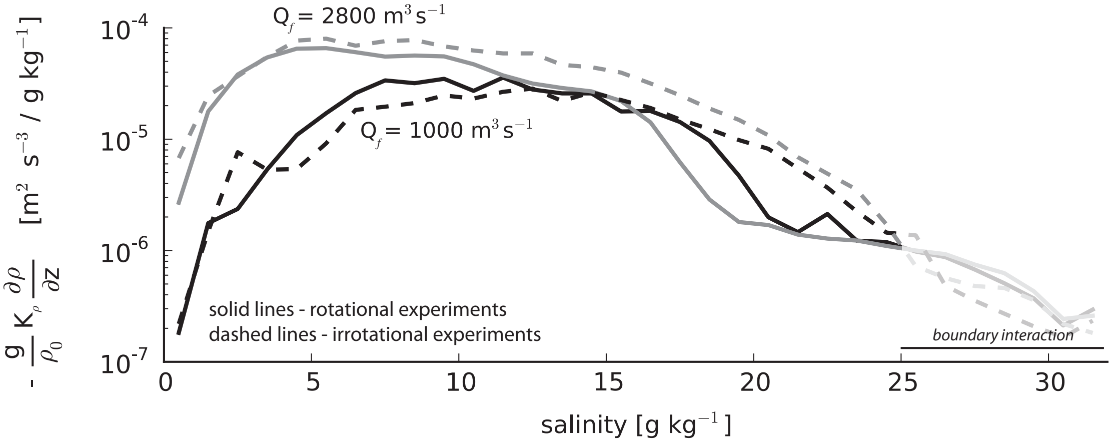

Figure 4.8: Mean (over ebb) isohaline vertical turbulent buoyancy flux for the $Q_f = 1000$ m^3 s^{-1} (black lines) and $Q_f = 2800$ m^3 s^{-1} (gray lines) experiments with (solid lines) and without (dotted lines) rotation. g is gravity, ρ_0 is the background density and K_ρ is the turbulent diffusion coefficient. The transparent region marks where isohalines interact with the offshore boundary in the irrotational cases.

4.3.2 Density changes in the near-field

In this section, net plume mixing in rotational and irrotational experiments is investigated using the change in density of a parcel of water as it traverses the plume. The peak salinity of fresh water storage (the salinity of water entering the coastal current) from the tidal mean differential fresh water volume distributions in Fig. 4.5 is used to estimate the far-field density anomaly and compared to the density anomaly of the inflow in rotational experiments.

The fresh water volume distribution for the $Q_f = 1000$ m^3 s^{-1} case without rotation shown in Fig. 4.5 reveals that there is no salinity with a local peak in fresh water volume because no coastal current forms. Without rotation, the plume continues to spread until it is mixed to the ambient salinity and pools in that isohaline. The rotational and irrotational simulations are fundamentally different in terms of density structure, and therefore the same methods cannot be used to evaluate net mixing in both cases. For the irrotational experiments, the far-field density anomaly is calculated by fitting an exponential decay function to the plume density anomaly along an offshore transect similar to the method described in Hetland (2010). The far-field density anomaly derived from the numerical experiments are compared to a similar metric evaluated from Halverson and Pawlowicz (2008). Because they are calculated in slightly different ways, the exact values of the far-field density anomaly should not be rigorously compared between the different model cases and the data, but it is reasonable to compare the trends between cases using these synonymous measures of net mixing because all definitions of the near-field scale similarly.

The gray region in Fig. 4.9 shows the density anomaly throughout the domain by radial distance from the mouth for the $Q_f = 500$ m^3 s^{-1} experiment without rotation. The density anomaly in this analysis is determined the same way as described in the previous section. The ambient flow and tides in this experiment result in two water masses that exhibit different trends offshore. Although these complexities are not present in the Hetland (2010) experiments, a comparable water mass representative of pure offshore radial spreading is evaluated, identified by the solid, bold black line. This line marks the tidal-mean density anomaly along a transect directly eastward in the offshore direction from the mouth, and falls within the water mass that exhibits a gentle grade in density anomaly from the estuary mouth to the offshore boundary, representing water flowing in the offshore-downcoast direction. Water spreading along this path leaves the domain before it reaches the ambient ocean salinity, since the plume is not confined to the domain by rotation.

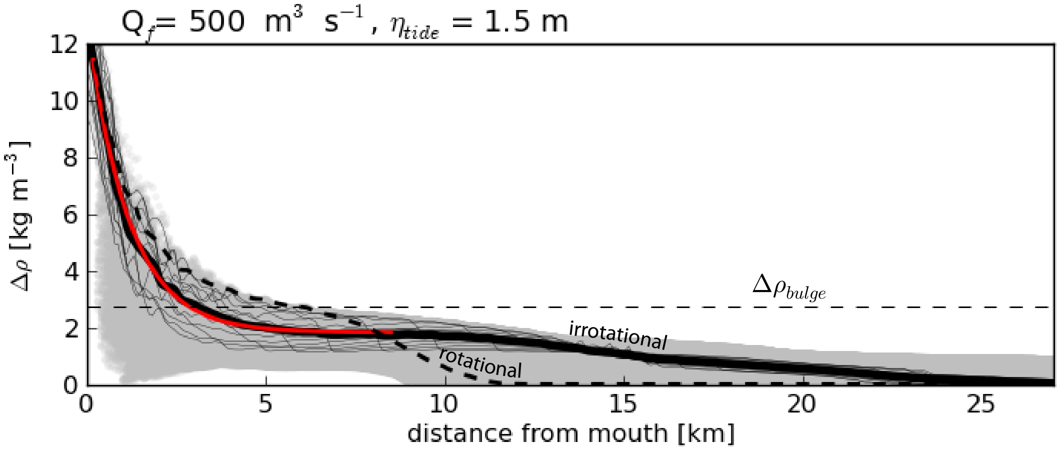

Figure 4.9: Grey shaded region is domain-wide upper layer density anomaly every hour over a tide for the $Q_f = 500$ m^3 s^{-1} experiment without rotation. Thick, black line is the tidal mean upper layer density anomaly over an offshore transect from the mouth. Thin, black lines show the tidal variability of the upper layer density anomaly over the transect. The red line is the fit of an exponential decay function to the density anomaly for the inshore portion of the transect. Thick, black, dashed line is the tidal mean upper layer density anomaly along the offshore transect for the $Q_f = 500$ m^3 s^{-1} experiment with rotation. Thin, black, dashed line marks the density anomaly of water entering the coastal current for the $Q_f = 500$ m^3 s^{-1} rotational experiment from Fig. 4.5.

The density anomaly at the offshore location where tidal variability is minimal (thin black lines in Fig. 4.9 show hourly tidal variability along the offshore transect) represents the far-field density anomaly in the tidally-pulsed, irrotational case. The offshore limit of an exponential decay function (red line in Fig. 4.9) fit to the upcoast portion of the curve where the concavity is positive is used to find this quantity. This method is used to find the far-field density anomaly for all of the experiments without rotation. The thick, dashed line in Fig. 4.9 shows the upper layer density anomaly along the same offshore transect for the $Q_f = 500$ m^3 s^{-1} simulation with rotation. Coastal trapping of the plume results in a non-exponential shape to the density anomaly offshore. Therefore, this method cannot be applied to the experiments with rotation; the far-field density anomaly determined from the differential fresh water volume distributions (Fig. 4.5) is a more reasonable estimate (shown by the thin, dotted line in Fig. 4.9).

Similar to Fig. 5 in Hetland (2010), net plume mixing is expressed as a ratio of the far-field density anomaly to the initial density anomaly at the estuary mouth ($\Delta\rho_{bulge}/\Delta\rho_i$) as a function of plume discharge rate in the top panel of Fig. 4.10 (the estuary mouth width, W_i, is kept constant in these numerical experiments). Note that the bulge is a rotational phenomenon, and in the rotational experiments $\Delta\rho_{bulge}$ is related to the density anomaly of the rotational bulge, but in irrotational experiments $\Delta\rho_{bulge}$ simply represents the density anomaly of plume water entering the far-field; they are labeled similarly for comparison. ($\Delta\rho_{bulge}/\Delta\rho_i$) is always less than one due to plume entrainment; the plume density offshore is greater than the plume density at the mouth, thus the density difference with respect to ambient water is smaller offshore. Less mixing has occurred if the ratio is near one. The variability of the individual components of $\Delta\rho_{bulge}/\Delta\rho_i$ are shown in the bottom panel of Fig. 4.10 to illustrate the relative contribution of the numerator and denominator.

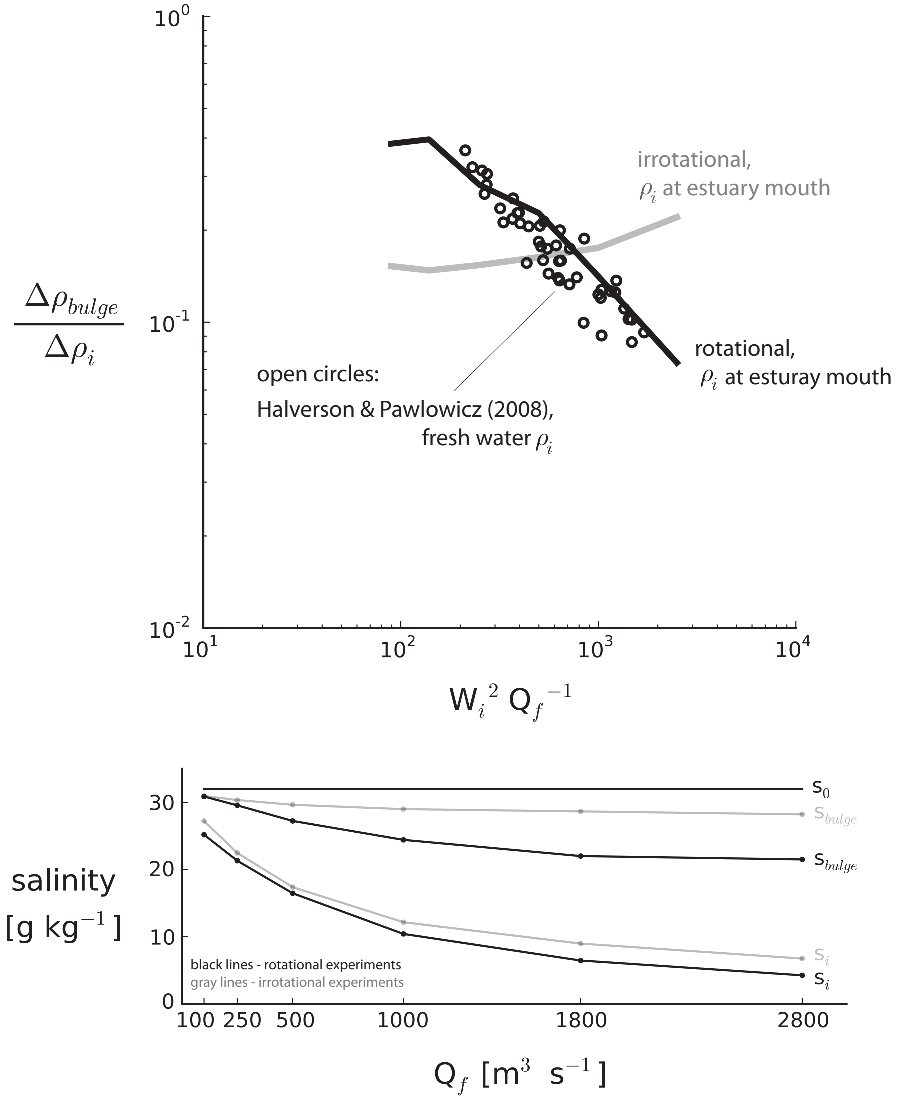

Figure 4.10: Top panel shows the ratio of the far-field density anomaly, $\Delta\rho_{bulge}$, to the inshore density anomaly, $\Delta\rho_i$ (either at the estuary mouth or river mouth), as a function of fresh water discharge, Q_f, and estuary mouth width, W_i. Lines use ρ_i at the estuary mouth and open circles use fresh water ρ_i. The black line represents rotational experiments and the isopycnal where peak fresh water storage occurs (Fig. 4.5) is used for ρ_{bulge}. The gray line displays irrotational experiments and the offshore limit of the exponential fit to the density anomaly (Fig. 4.9) is used for $\Delta\rho_{bulge}$. Open circles are calculated from plume and reference salinity data from Halverson and Pawlowicz (2008).

Three variations of this estimate are evaluated and shown in the top panel of Fig. 4.10. Recall that ρ_{bulge} is the isopycnal where peak fresh water storage occurs (Fig. 4.5) for the experiments with rotation and $\Delta\rho_{bulge} = \rho_0$ - ρ_{bulge} is the offshore limit of the exponential fit to the density anomaly (Fig. 4.9) for the experiments without rotation. $\Delta\rho_i = \rho_0$ - ρ_i is the density anomaly at the estuary mouth given by the exponential decay function in the irrotational experiments. ρ_0 is the ambient density (from $s_0 = 32$ g kg^{-1}) and ρ_i is the tidally averaged, transport wighted mean density of outflowing water at the estuary mouth in the rotational experiments. The gray line in the top panel of Fig. 4.10 illustrates the trend in net plume mixing with changing discharge in the irrotational experiments and the black line shows the net mixing trend in rotational experiments.

The black, open circles show the net mixing trend from observational data described in Halverson and Pawlowicz (2008). Mean Fraser plume salinity and reference salinity are reported as a function of river discharge rate over ~4 years (Fig. 5 in Halverson and Pawlowicz (2008)). These data are collected by a ferry that traverses the Strait of Georgia four times daily. The ferry track is ~50 km long in the along-strait direction and ~15 km from the main mouth of the Fraser at it's closest point. The Fraser discharge is seasonally variable, but can be as high as 9000 m^3 s^{-1} at spring freshet; the riverine water is extensive in the strait and manifest in the ferry measurements. Details of how the plume boundary is chosen are explained in Appendix B of Halverson and Pawlowicz (2008). To relate these data to net plume mixing, the density anomaly is calculated from the salinity observations (used to calculate ρ_{bulge} and ρ_0). No information at the river mouth is available in Halverson and Pawlowicz (2008), so we compare the plume density anomaly to the fresh water density anomaly. This is reasonable, since fresh water often reaches the mouth during moderate ebb discharges. The width of the Fraser estuary mouth is assumed to be ∼1 km; the geometry of the mouth is relatively complex, with a jetty to the north and tidal flats to the south that extend ∼1.5 km further offshore than the jetty. Although the channel is narrow, the bathymetric break (defined by the 12 m depth contour), and thus the salt front, follow an ∼1 km diagonal across the mouth from the edge of the tidal flats to nearly the end of the jetty (MacDonald and Geyer, 2005).

Recall that it is the slopes of the different cases that are of interest, rather than the actual values of the far-field density anomaly. The open circles and black line exhibit a similar trend, implying that in a geophysical scale plume, as river discharge increases, net plume mixing decreases. Without rotation, the spreading region is extensive and shear-mixing occurs over a larger interfacial area, producing the opposite trend in net plume mixing displayed by the gray line, as hypothesized by Hetland (2010).

4.4 Discussion

Numerical experiments in this study address the net mixing response of a river plume to increasing fresh water discharge in an effort to explain the disagreement in existing literature. Our experiments produce results in agreement with both Halverson and Pawlowicz (2008) and Hetland (2010) depending on if rotation is included, or not, thus explaining the contradiction. As river discharge is added to the estuary-plume system, the net mixing in a geophysical scale plume influenced by rotation will decrease and in an irrotational plume the net mixing will increase. We explain this difference as an effect of rotation decelerating the plume and limiting the size of the near-field where shear mixing occurs. Conversely, the near-field area grows linearly with discharge in irrotational experiments. Fig. 4.3 indicates a fundamentally different horizontal density structure between rotational and irrotational experiments, so different trends in net plume mixing are expected.

The upper panel of Fig. 4.10 shows contrasting trends in $\Delta\rho_{bulge}/\Delta\rho_i$ between the rotational and irrotational cases. The relative increase or decrease of the individual terms $\Delta\rho_{bulge}$ and $\Delta\rho_i$ is difficult to infer from the upper panel of Fig. 4.10, so s_i and s_{bulge} (inflow and bulge salinities) are shown separately as a function of discharge rate in the bottom panel of Fig. 4.10. Both s_i and s_{bulge} freshen with increasing discharge in rotational and irrotational experiments, but the freshening effect of the added buoyancy is greater in the rotational case. Although the local shear mixing is stronger with higher discharge, it is not enough to fully mix the added fresh water to near-ocean salinities before it enters the coastal current; this is reflected in the freshening of the differential freshwater volume curves with increasing discharge in Fig. 4.5 and the isohaline surface area curves in Fig. 4.6. The bottom panel of Fig. 4.10 also shows that s_i is consistently saltier in the irrotational cases, presumably from altered estuarine mixing in a rotation-free environment. Lastly, s_i freshens with discharge faster than s_{bulge} in both cases, but s_{bulge} freshens at nearly the same rate as s_i in the rotational case.

Fig. 4.7 and Fig. 4.8 display the isohaline variability in the rotational arrest of the near-field with discharge rate. Although jet inertia pushes the geospatial location of the near-field arrest further offshore in high discharge plumes (compare high and low discharge plumes in Fig. 4.2), the added inflow buoyancy causes the rotational arrest to occur in fresher isohalines relative to low discharge plumes. In irrotational cases, the plume spreading is not inhibited by rotation; the transition to the far-field happens farther offshore and the source water has undergone more mixing. Fig. 4.8 also shows that at low salinities, local mixing rates are elevated near the inflow in high discharge plumes; an effect of increased discharge velocity and buoyant spreading. Also, at fresher salinity classes, before rotation takes effect, the mixing rates are similar for experiments with the same discharge. In rotational cases however, the increased buoyancy flux into the plume with high discharge is more than can be mixed to the ambient salinity before rotation arrests the spreading, leading to a net freshening of the plume.

The parameter dependence of the advective time scale in the near-field suggests that net mixing is sensitive to discharge, and comparison of the advective time scale to the rotational time scale indicates the similarity between the two. The supercritical Froude number criterion gives $Fr^2 = u^2/g'h \simeq 1$ at the lift off point. This relation, combined with $Q_f = uhW$ at the estuary mouth, gives

$$U \sim (\frac{g'Q_f}{W})^{\frac{1}{3}} \tag{4.8}$$

as a scale for the inflow velocity.

Fig. 10 in Halverson and Pawlowicz (2008) indicates a roughly linear relationship between plume surface area, A_{plume}, and river discharge, e.g. $A_{plume} \sim c_A^{-1} Q_f$, where $c_A \sim 6.7 \text{ x } 10^{-6}$ m s^{-1}. Therefore $L \sim (c_A^{-1} Q_f)^{\frac{1}{2}}$, where L is the length scale associated with the inflow. As in this study, Hetland (2005) relates plume isohaline surface area to discharge rate and entrainment, therefore the physical meaning of c_A is a mean vertical entrainment velocity over isohaline surface area A (see Eq. (4.1), c_A is equivalent to w_e). This estimate of entrainment velocity falls at the low end of the range of values shown in Fig. 3 in Hetland (2010); it is small for near-field mixing. However, smaller values are expected for the mean vertical entrainment velocity since the very high mixing regions of the plume occur in a very small fraction of the total plume area. Similarly, Halverson and Pawlowicz (2011) calculate low values of entrainment in the new-field of the Fraser plume because of spatial and time averaging. The empirical relationship reported between river discharge and plume area in

Fig. 10 in Halverson and Pawlowicz (2008) is likely also sensitive to stratification at the river mouth, and the addition of a proportional density coefficient would offer a more reasonable near-field entrainment velocity estimate; e.g. $L \sim (w_e^{-1} \frac{\Delta\rho}{\Delta\rho_f} Q_f)^{\frac{1}{2}}$. A measure of stratification would provide physical clarity, but it is not necessary for the following scaling arguments.

A translational timescale related to advection, L/U, which describes the time it takes for a particle to traverse the near-field plume, may be derived using the length and velocity scales of the plume derived above,

$$T \sim \frac{Q_f^{\frac{1}{6}} W^{\frac{1}{3}}}{g'^{\frac{1}{3}} c_A^{\frac{1}{2}}}, \tag{4.9}$$

implying that $T \propto Q^{\frac{1}{6}} W^{\frac{1}{3}}$, which are the inflow variables considered in Fig. 4.10 that impact net plume mixing. Thus as discharge increases, the quantity of water released expands the near-field faster than it speeds up the flow, increasing the time scale (U scale s as $Q^{\frac{1}{3}}$ in Eq. (4.8) and L scales as $Q^{\frac{1}{2}}$). Furthermore, as the mouth width increases, the outflow is less constricted, leading to a weaker jet and a longer time scale; mouths that are much wider than the deformation radius are not constricting and likely do not produce a near-field plume. Applying 5000 m^3 s^{-1} for Q_f, 1000 m for W and 0.25 m s^{-2} for g', gives the translational time scale for the Fraser inflow as $T \sim 7$ hrs. Furthermore, $Tf \sim 2.5$, indicating that the translational time scale exceeds the rotational time scale and rotation plays a role in limiting near-field spreading.

Hetland (2005) describes the advective-diffusive balance in the plume, assuming a steady river discharge and salinity field, as

$$s_A Q_f = -\int_A \mathbf{F} \cdot \hat{\mathbf{n}}\, \mathbf{dA}. \tag{4.10}$$

The physical meaning of Eq. (4.10) is that fresh water added at the river end of an isohaline volume is balanced by the turbulent flux of fresh water $\mathbf{F}/\mathbf{s_A}$ across the surface of the isohaline volume. In Fig. 4.5, the near-/mid-field is identified in isohaline space by the region of generally increasing fresh water volumes (or isohaline surface area in Fig. 4.6) moving to higher salinities, indicating fresh water flushing to saltier isohalines. The time scale of the inflow estimated above is related to the flushing time of the largest isohalines in this range. The peak in fresh water storage marks the salinity where spreading is arrested by rotation and mixing to higher salinities is minimal. The $Q_f = 1000$ m^3 s^{-1} irrotational case in Fig. 4.5 shows that the translational time scale exceeds the rotational time scale, as fresh water is mixed to higher salinities even in the isohalines with large flushing times.

The tidal pulsing and ambient flow in the experiments support a different physical environment than the steady, pure radial spreading plume experiments described in Hetland (2010). The addition of realistic physical forcing allows comparison with field data, as rotation, tides and ambient currents are important elements to the Fraser plume evolution. Halverson and Pawlowicz (2008) suggest that wind driven circulation in the Strait of Georgia is different than the shelf plume response because of the ambient currents in the enclosed strait, so we exclude wind forcing from our current experiments. We assume that interfacial stress is much larger than wind stress in the near-field and justify the absence of wind by the results of previous studies that show wind effects are secondary near the river mouth. Furthermore, observations of mixing in the near-field of the Merrimack River plume in the springs of 2010 and 2011, intended to support these model results, were measured during calm, as there is currently no evidence that wind forcing is important in the near-field. We assert that the added complexity of wind forcing is unnecessary; the experiments in this paper explain the results of existing literature, focusing only on shear mixing through the near-/mid-field region.

4.5 Conclusion

This study demonstrates net mixing trends in a discharge varying, buoyant coastal plume with a constricted mouth. The primary finding of this study is that rotation is effective in limiting plume spreading, and therefore reduces net shear mixing in the near-field. The arrest of the interfacial shear mixing region by rotation results in water leaving the near-field plume that is not as modified as an advective measure, such as the jet-to-plume length scale, would predict.

Besides illustrating the impact of rotation on net mixing, these experiments elucidate net mixing trends in plumes with time dependent estuarine discharge; the results of this study are especially pertinent to plumes with highly variable discharge, such as the Eel River plume in northern California, that exhibit source flux variability across several orders of magnitude. The combined effect of rotation and increasing discharge leads to less net mixing, while the effect of increasing discharge and the absence of rotation leads to greater net mixing. Increasing transport at the river mouth strengthens mixing in the discharge jet near the source, and increasing buoyancy input enhances the spreading of the plume while perpetuating shear mixing, ergo an increasingly mixed far-field plume with increasing discharge in an irrotational environment. However, in a rotational environment, rotation begins to act on the flow in the plume several mouth widths offshore, redirecting the flow downcoast and curbing shear mixing while preventing further radial spreading, resulting in a more stratified far-field plume. Rotation arrests mixing in the near-field plume by reducing the rate of spreading, so that the plume leaving the near-field is fresher than it would be without rotation.

Inconsistent reports of net plume mixing are reported in previous literature, and the experiments in this study provide a framework for understanding these prior results. To date, rotational effects are not heavily weighted in studies of near-field plume structure because local shear mixing is not significantly affected by rotation. However, to provide a realistic representation of early plume evolution, rotation is a critical element to include in a near-field model; the rotational parameter will alter near-field density and plume depth by suppressing spreading, and therefore when and where a plume transitions to subcritical. The far-field density anomaly provides the boundary condition for the coastal current and offshore shelf circulation, so an understanding how much mixing happens in the near-field provides a link between plume studies focussed on the two regions, and furthermore, bridges engineering and geophysical scale studies.

5. CONCLUSION

The importance of tides, discharge and rotation in the mid-field transition is addressed in this dissertation. Both the deceleration of the plume body through mixing and the relaxation of the tidal plume front are examined. Realistic and idealized numerical simulations are used to address the hypotheses stated in Section 1.3.

There are three main findings in this research. First, ∼6.5% of the ebb discharge interacts with the tidal plume front, verifying the second statement of hypothesis II. Interfacial mixing over the expanding plume body and the narrow region of overtaking velocities confined to the plume core result in the small fraction of source water to reach the front. Also, source water released after ∼3 hours into ebb does not interact with the propagating front, therefore frontal mixing can only account for mixing this small portion of early ebb discharge. The connection between the mouth and the front does not end during ebb, as predicted in hypothesis I. Source water moves frontward even after the tidal plume begins to recirculate and transition to the far-field, but only water released early in ebb interacts with the tidal plume front. Extrapolating these results to infer the time evolution of frontal structure, this analysis indicates that the front is most bore-like during early ebb; as ebb progresses this structure diminishes and less source water is mixed through it.

The second important finding in this research is that the mouth and the front communicate on an advective time scale. When the estuarine discharge is stopped, the front does not respond by slowing until it experiences the absence of the obstructed source water, indicating that the inertia of the discharge already released is enough to keep it moving frontward. However, the separation of the fronts with and without stopping the discharge is minimal, supporting the second statement of hypothesis I. The time dependent ebb discharge does impact frontal propagation to some extent, as previous studies have shown, but with a lag as water travels through the plume. The initial formation of the front appears to be critical in setting it's propagation speed, as the increased supply of source water to the frontal region in the case with realistic ebb discharge does not greatly change the front speed relative to the case where discharge is stopped.

Since the waning ebb discharge does not strongly impact the relaxation of the front, the impact of rotation in slowing the plume is investigated. The third discovery in this research is that when discharge is increased, rotational and irrotational plumes exhibit different trends in net plume mixing, defined as the cumulative mixing of a parcel of source water before it enters the far-field. This result supports hypothesis III. Rotation turns the plume, arresting spreading and limiting mixing, leading to less mixed water entering the far-field. This analysis explains the results of previous experiments and links engineering and geophysical scale studies of near-field plumes.

There are several unanswered questions in this research, mainly surrounding the role of wind in the mid-field transition. Previous studies assume that wind is of little importance in driving the near-field, but efforts to address wind advection and mixing during early plume formation in the Merrimack is ongoing with colleagues. Furthermore, innovative observational and modeling studies of plume mixing by surface waves during certain wind conditions are proposed.

Many advances in river plume understanding have been achieved in the last decade, but several fundamental questions remain. Ongoing numerical, laboratory and field investigations look promising to answer these questions. Many questions specific to narrow mouth, tidally pulsed plumes are front-focused. Where does source water go after it is cycled through the front? Is a front-focused model reasonable to simulate tidal plume evolution, or do the dynamics of the entire tidal plume need to be modeled? Is mixing in the interior of the plume different because of the front? Currently, there are efforts to investigate the temporal evolution of front structure from observations and non-hydrostatic models. The generation and propagation of internal waves through the plume and ebb-to-ebb interaction of these waves with previous tidal pulses stratifying shelf waters is another non-hydrostatic topic of present interest.

Both modelers and observationalists recognize the broad array of mixing processes in the tidal plume alone. Observations are integral for measuring local mixing, but estimation of global plume parameters over many tidal cycles must be achieved through models. An essential avenue of plume research is determining when, where and how mixing happens and the variability in and between systems; future research will greatly benefit from an analysis of the plume energy budget.

As a whole, river plumes have a baseline similar behavior, but estuarine and coastal circulation varies considerably form one system to another. There are several paradigms for the entrance of fresh water to the ocean dependent on the physical environment of the region. Estuarine dynamics are variable because the effect of tides and discharge is magnified in small, enclosed regions. The type of estuary is determined by it's geometry and bathymetry, which greatly influences mixing time scales and time scales of adjustment to changes in forcings that are difficult to predict. It is interesting to note that while estuarine environments are vastly different, plume behavior is similar amongst most regions of freshwater influence. Far from the river mouth this is especially true. Even in the presence of tides, mixing in most near-field plumes is fairly well understood and predictable; it can be distilled down to dependence on inflow variables that drive spreading and shear mixing. Mixing in the far-field is even better understood; wind mixes the plume to a depth dependent on a critical bulk richardson number, producing predictable far-field plume structure. This is why the far field plume is decently resolved in large scale models; the unresolved details of mixing in the estuary and near-field are forgiven once the wind takes hold of the plume, which typically happens within tens of kilometers from the river mouth.

While new studies focused on poorly understood systems will be fruitful, there is need to synthesize existing knowledge from recent large river plume studies and better define a map of parameter space, or relevant nondimensional variables, that enables the collapse of data from many systems. This will allow a framework for comparison between plume regimes and will help identify temporal variability in a single system. Is it possible to scale up one system to reflect another? How does mixing relate to the scale of the discharge? Why does data from some plumes, like the Columbia, not collapse well? Enough work in different systems has been done that these big-picture questions have recently gained attention and are ripe to answer. Note that a similar approach should be taken to understand the estuarine and far-field shelf circulations and it is possible that many relevant variables classifying plumes are related to dynamic variables in these regions, as the plume is the connection between the two.

Overall, the research presented in this dissertation provides direction for future plume studies though increased understanding of buoyancy driven flow in the coastal ocean and can be used to improve the predictive capabilities of models of the spatial structure and temporal evolution of tidally modulated river plumes and the associated shelf circulation. It has several engineering applications; for example, new information about mixing, spreading and the transmission of source water form the mouth to the front in a coastal plume is provided that can aid in nearshore management in the event of estuarine derived pollutants entering the coastal ocean. Furthermore, increased understanding of plume physical processes introduces a range of new broader impact, interdisciplinary questions; for example, what is the ecological impact of the convergence of chemical and biological materials in the front? As a whole, this research answers several scientific questions regarding early plume formation and contributes to our knowledge of mid-field plume processes.

REFERENCES

Allison, M., Alongi, D., Bi, N., Bianchi, T., Billen, G., Blair, N., Bombar, D., Borges, A., Bouillon, S., Broussard, G., Cai, W.-J., Callens, J., Chakraborty, S., Arthur Chen, C., Chen, N., Corbett, D., Dai, M., Day, J., Dippner, J., Duan, S., Duarte, C. Eglinton, T., Erkens, G., France-Lanord, C., Gaillardet, J., Galy, V., Gan, J., Gariner, J., Goni, M., Gundersen, K., Guo, L., Nhu Hai, D., Han, A., Harrison, P., Hein, C., Hernes, P., Hetland, R., Holmes, R., Hsu, T., Hunsinger, G., Kolker, A., Kung, H., Lai, Z., Ngoc Lam, N., Leithold, E., Liu, P., Lohrenz, S., Loick-Wilde, N., Macdonald, R., Meselhe, E., Middelkoop, H., Mitra, S., McKee, B., Moufaddal, W., Murrell, M., Nittouer, C., Ogston, A., Passy, P., van der Perk, M., Ramanathan, A., Raymond, P., Robertson, A., Rosenheim, B., Shaffer, G., Shiller, A., Silvestre, M., Spencer, R., Striegl, R., Stubbins, A., Tank, S., Thieu, V., Visser, J., Voss, M., Walsh, J., Wang, H., Woerner, W., Wu, Y., Xu, J., Yang, Z., Yin, K., Yin, Z., Zhang, G., Zhang, J., Zhu, Z., and Zimmerman, A. (2014). Fresh water and sediment dispersal in large river plumes. In Bianchi, T., Allison, M., and Cai, W.-J., editors, *Biogeochemical dynamics at major river-coastal interfaces: Linkages with global change*. Cambridge University Press, New York, NY.

Armi, L. and Farmer, D. (1986). Maximal two-layer exchange through a contraction with barotropic net flow. *J. Fluid Mech.*, 164:27–51.

Bigelow, H. B. (1927). *Physical oceanography of the Gulf of Maine*. US Government Printing Office.

Britter, R. E. and Simpson, J. E. (1978). Experiments on the dynamics of a gravity current head. *J. Fluid Mech.*, 88:223–240.

Brooks, D. A. (1985). Vernal circulation in the Gulf of Maine. *J. Geophys. Res.*, 90(C3):4687–4706.

Brooks, D. A. (1994). A model study of the buoyancy-driven circulation in the Gulf of Maine. *J. Phys. Oceanogr.*, 24(11):2387–2412.

Brown, W. S. (1998). Wind-forced pressure response of the Gulf of Maine. *J. Geophys. Res.*, 103(C13):30661–30678.

Brown, W. S. and Beardsley, R. C. (1978). Winter circulation in the western Gulf of Maine: Part 1. Cooling and water mass formation. *J. Phys. Oceanogr.*, 8(2):265–277.

Bumpus, D. F. and Lauzier, L. M. (1965). Surface circulation on the continental shelf off eastern North America between Newfoundland and Florida. In *Serial Atlas of the Marine Environment*. American Geographical Society.

Canuto, V., Howard, A., Cheng, Y., and Dubovikov, M. (2001). One-point closure model - momentum and heat vertical diffusivities. *J. Phys. Oceanogr.*, 31:1413–1426.

Chapman, D. (1985). Numerical treatment of cross-shelf open boundaries in a barotropic coastal ocean model. *J. Phys. Oceanogr.*, 15:1060–1075.

Chapman, D. C. and Lentz, S. J. (1994). Trapping of a coastal density front by the bottom boundary layer. *J. Phys. Oceanogr.*, 24(7):1464–1479.

Chapman, D. C. and Lentz, S. J. (1997). Adjustment of stratified flow over a sloping bottom. *J. Phys. Oceanogr.*, 27(2):340–356.

Chen, F. and MacDonald, D. (2006). Role of mixing in the structure and evolution of a buoyant discharge plume. *J. Geophys. Res.*, 111(C11002).

Chen, F., MacDonald, D., and Hetland, R. (2009). Lateral spreading of a near -field river plume: Observations and numerical simulations. *J. Geophys. Res.*, 114(C07013).

Chen, S.-N., Geyer, W. R., Ralston, D. K., and Lerczak, J. A. (2012). Estuarine exchange flow quantified with isohaline coordinates: contrasting long and short estuaries. *J. Phys. Oceanogr.*, 42(5):748–763.

Choi, B.-J. and Wilkin, J. L. (2007). The effect of wind on the dispersal of the Hudson River plume. *J. Phys. Oceanogr.*, 37(7):1878–1897.

Chu, C.-k. (1997). *Mixing of turbulent advected line puffs*. PhD thesis, University of Hong Kong.

Covich, A., Falkenmark, M., Gleick, P., Lindh, G., McCaffrey, S., Nash, L., Postel, S., and Shiklomanov, I. (1993). World fresh water resources. In Gleick, P., editor, *Water in crisis: A guide to the world's fresh water resources*. Oxford University Press, New York, NY.

Dyer, K. (1997). *Estuaries: A physical introduction*. John Wiley & Sons, Chichester, England, 2 edition.

Flather, R. (1976). A tidal model of the northwest European continental shelf. *Memoires de la Societe Royale des Sciences de Liege*, 10(6):141–164.

Fong, D. A. and Geyer, W. R. (2001). Response of a river plume during an upwelling favorable wind event. *J. Geophys. Res.*, 106(C1):1067–1084.

Fong, D. A. and Geyer, W. R. (2002). The alongshore transport of freshwater in a surface-trapped river plume. *J. Phys. Oceanogr.*, 32(3):957–972.

Garcia Berdeal, I., Hickey, B., and Kawase, M. (2002). Influence of wind stress and ambient flow on a high discharge river plume. *J. Geophys. Res.*, 107(C9):13–1.

Garvine, R. (1982). A steady state model for buoyant surface plume hydrodynamics in coastal waters. *Tellus*, 34:293–306.

Garvine, R. (1987). Estuary plumes and fronts in shelf waters: A layer model. *J. Phys. Oceanogr.*, 17:1877–1896.

Garvine, R. W. (1984). Radial spreading of buoyant, surface plumes in coastal waters. *J. Geophys. Res.*, 89:1989–1996.

Garvine, R. W. (1995). A dynamical system for classifying buoyant coastal discharges. *Cont. Shelf Res.*, 15(13):1585–1596.

Garvine, R. W. and Monk, J. D. (1974). Frontal structure of a river plume. *J. Geophys. Res.*, 79(15):2251–2259.

Geyer, W., Signell, R., Fong, D., Wang, J., Anderson, D., and Keafer, B. (2004). The freshwater transport and dynamics of the western Maine coastal current. *Cont. Shelf Res.*, 24(12):1339–1357.

Geyer, W. R., Scully, M. E., and Ralston, D. K. (2008). Quantifying vertical mixing in estuaries. *Environ. Fluid Mech.*, 8(5-6):495–509.

Halverson, M. and Pawlowicz, R. (2008). Estuarine forcing of a river plume by river flow and tides. *J. Geophys. Res.*, 113(C09033).

Halverson, M. and Pawlowicz, R. (2011). Entrainment and flushing time in the Fraser River estuary and plume from a steady salt balance analysis. *J. Geophys. Res.*, 116(C8).

Hetland, R. (2005). Relating river plume structure to vertical mixing. *J. Phys. Oceanogr.*, 35:1667–1688.

Hetland, R. (2010). The effects of mixing and spreading on density in near-field river plumes. *Dyn. Atmos. Oceans*, 49(1):37–53.

Hetland, R. and MacDonald, D. (2008). Spreading in the near-field Merrimack River plume. *Ocean Modell.*, 21:12–21.

Hetland, R. D. and DiMarco, S. F. (2008). How does the character of oxygen demand control the structure of hypoxia on the Texas–Louisiana continental shelf? *J. Mar. Syst.*, 70(1):49–62.

Horner-Devine, A., Jay, D., Orton, P., and Spahn, E. (2009). A conceptual model of the strongly tidal Columbia River plume. *J. Mar. Syst.*, 78:460–475.

Huq, P. (2009). The role of Kelvin number on bulge formation from estuarine buoyant outflows. *Estuaries Coasts*, 32(4):709–719.

Jay, D. A., Pan, J., and Horner-Devine, A. R. (2009). Asymmetry of Columbia River tidal plume fronts. *J. Mar. Syst.*, 78:442–459.

Jay, D. A., Zaron, E. D., and Pan, J. (2010). Initial expansion of the Columbia River tidal plume: Theory and remote sensing observations. *J. Geophys. Res.*, 115(C00B15).

Jirka, G. (2007). Buoyant surface discharges into water bodies. II: Jet integral model. *J. Hydrol. Eng.*, 133(9):1021–1036.

Jirka, G. H. (2004). Integral model for turbulent buoyant jets in unbounded stratified flows. part i: Single round jet. *Environ. Fluid Mech.*, 4(1):1–56.

Jones, G., Nash, J., Doneker, R., and Jirka, G. (2007). Buoyant surface discharges into water bodies. I: Flow classification and prediction method. *J. Hydrol. Eng.*, 133(9):1010–1020.

Kashiwamura, M. and Yoshida, S. (1967). Outflow pattern of fresh water issued from a river mouth. *Coastal Eng. Japan*, 10:109–115.

Kilcher, L. F. and Nash, J. D. (2010). Structure and dynamics of the Columbia River tidal plume front. *J. Geophys. Res.*, 115(C05S90).

Kilcher, L. F., Nash, J. D., and Moum, J. N. (2012). The role of turbulence stress divergence in decelerating a river plume. *J. Geophys. Res.*, 117(C5).

Kundu, P. (1990). *Fluid Mechanics*. Academic Press, San Diego, CA.

Largier, J. L. (1992). Tidal intrusion fronts. *Estuaries*, 15(1):26–39.

Lentz, S. J. and Helfrich, K. R. (2002). Buoyant gravity currents along a sloping bottom in a rotating fluid. *J. Fluid Mech.*, 464:251–278.

Luketina, D. A. and Imberger, J. (1987). Characteristics of a surface buoyant jet. *J. Geophys. Res.*, 92(C5):5435–5447.

MacCready, P. (1999). Estuarine adjustment to changes in river flow and tidal mixing. *J. Phys. Oceanogr.*, 29(4):708–726.

MacCready, P. (2007). Estuarine adjustment. *J. Phys. Oceanogr.*, 37(8):2133–2145.

MacCready, P., Banas, N. S., Hickey, B. M., Dever, E. P., and Liu, Y. (2009). A model study of tide-and wind-induced mixing in the Columbia River estuary and plume. *Cont. Shelf Res.*, 29(1):278–291.

MacCready, P., Hetland, R., and Geyer, W. (2002). Long-term isohaline salt balance in an estuary. *Cont. Shelf Res.*, 22:1591–1601.

MacDonald, D. and Geyer, W. (2004). Turbulent energy production and entrainment at a highly stratified estuarine front. *J. Geophys. Res.*, 109(C05004).

MacDonald, D. and Geyer, W. (2005). Hydraulic control of a highly stratified estuarine front. *J. Phys. Oceanogr.*, 35:374–387.

MacDonald, D., Goodman, L., and Hetland, R. (2007). Turbulent dissipation in a near-field river plume: A comparison of control volume and microstructure observations with a numerical model. *J. Geophys. Res.*, 112(C07026).

Marchesiello, P., McWilliams, J. C., and Shchepetkin, A. (2001). Open boundary condition for long-term integration of regional oceanic models. *Ocean Modeling*, 3:1–20.

Marmorino, G. O. and Trump, C. L. (2000). Gravity current structure of the Chesapeake Bay outflow plume. *J. Geophys. Res.*, 105(C12):28847–28861.

McCabe, R., Hickey, B., and MacCready, P. (2008). Observational estimates of entrainment and vertical salt flux in the interior of a spreading river plume. *J. Geophys. Res.*, 113(C08027).

McCabe, R., MacCready, P., and Hickey, B. (2009). Ebb tide dynamics and spreading of a large river plume. *J. Phys. Oceanogr.*, 39(11):2839–2856.

Münchow, A. and Garvine, R. W. (1993). Dynamical properties of a buoyancy-driven coastal current. *J. Geophys. Res.*, 98(C11):20063–20077.

O'Donnell, J. (1990). The formation and fate of a river plume: A numerical model. *J. Phys. Oceanogr.*, 20:551–569.

O'Donnell, J., Marmorino, G. O., and Trump, C. L. (1998). Convergence and downwelling at a river plume front. *J. Phys. Oceanogr.*, 28:1481–1495.

Orlanski, I. (1976). A simple boundary condition for unbounded hyperbolic flows. 21:251–269.

Orton, P. and Jay, D. (2005). Observations at the tidal plume front of a high-volume river outflow. *Geophys. Res. Lett.*, 32(L11605).

Pritchard, M. and Huntley, D. (2006). A simplified energy and mixing budget for a small river plume discharge. *J. Geophys. Res.*, 111(C03019).

Ralston, D. K., Geyer, W. R., and Lerczak, J. A. (2010a). Structure, variability, and salt flux in a strongly forced salt wedge estuary. *J. Geophys. Res.*, 115(C6).

Ralston, D. K., Geyer, W. R., Lerczak, J. A., and Scully, M. (2010b). Turbulent mixing in a strongly forced salt wedge estuary. *J. Geophys. Res.*, 115(C12).

Scotti, A. and Pineda, J. (2007). Plankton accumulation and transport in propagating nonlinear internal fronts. *J. Mar. Res.*, 65:117–145.

Shchepetkin, A. and McWilliams, J. (2005). The regional oceanic modeling system (ROMS): A split-explicit, free-surface, topography-following-coordinate oceanic model. *Ocean Modell.*, 9(4):347–404.

Smolarkiewicz, P. and Clark, T. (1986). The multidimensional positive definite advection transport algorithm: Further development and applications. *J. Comp. Phys.*, 67(2):396–438.

Trenberth, K. E., Smith, L., Qian, T., Dai, A., and Fasullo, J. (2007). Estimates of the global water budget and its annual cycle using observational and model data. *J. Hydrometeor.*, 8(4):758–769.

Turner, R. E. and Rabalais, N. N. (1994). Coastal eutrophication near the Mississippi River Delta. *Nature*, 368:619–621.

Umlauf, L., Arneborg, L., Burchard, H., Fiekas, V., Lass, H., Mohrholz, V., and Prandke, H. (2007). Transverse structure of turbulence in a rotating gravity current. *Geophys. Res. Lett.*, 34(L08601).

Valle-Levinson, A. (2008). Density-driven exchange flow in terms of the Kelvin and Ekman numbers. *J. Geophys. Res.*, 113(C4).

Whitney, M. M. and Garvine, R. W. (2005). Wind influence on a coastal buoyant outflow. *J. Geophys. Res.*, 110(C3):C03014.

Wright, L. and Coleman, J. (1971). Effluent expansion and interfacial mixing in the presence of a salt wedge, Mississippi River Delta. *J. Geophys. Res.*, 76(36):8649–8661.

Yankovsky, A. and Chapman, D. (1997). A simple theory for the fate of buoyant coastal discharges. *J. Phys. Oceanogr.*, 27:1386–1401.

Yankovsky, A. E., Hickey, B. M., and Münchow, A. K. (2001). Impact of variable inflow on the dynamics of a coastal buoyant plume. *J. Geophys. Res.*, 106(C9):19809–19824.

Zhang, W. G., Wilkin, J. L., and Chant, R. J. (2009). Modeling the pathways and mean dynamics of river plume dispersal in the New York Bight. *J. Phys. Oceanogr.*, 39(5):1167–1183.

Zhong, L. and Li, M. (2006). Tidal energy fluxes and dissipation in the Chesapeake Bay. *Cont. Shelf Res.*, 26(6):752–770.